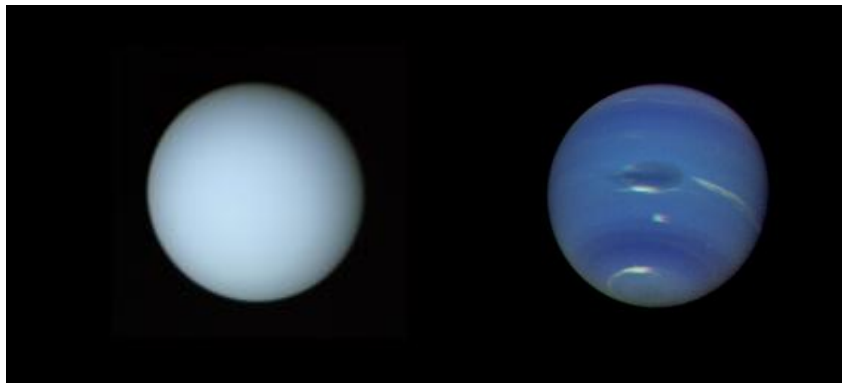


Remote Sounding of the Atmospheres of Uranus and Neptune



Dane Steven Tice

First Year Report

Lincoln College
Atmospheric, Oceanic and Planetary Physics
University of Oxford



August 2010

Word Count: ~13,800

Abstract

Our solar system's 'ice giant' planets, Uranus and Neptune, are unique among the planets orbiting the Sun. Huge spheres of gas like all four giant planets, the ice giants possess unique dynamics and properties which are derived from their cold temperatures and high abundances of water and methane (CH_4). Uranus' large obliquity and extremely weak internal heat source create a planet with dynamics controlled almost completely by solar forcing. Neptune's large inner heat flux and high water content create a planet with intensely turbulent circulation and highly active storm features. This report describes the techniques of remote sensing and retrieval theory as a means to study these fascinating and unique bodies. A summary is provided of ice giant knowledge to date, relying on the sparse collection of telescope and satellite data that has been analyzed. New telescope data in the near-IR promises a means of further interpreting these planets, where no *in situ* results have ever been obtained, and our knowledge is rudimentary. Preliminary analysis of telescope data from NASA's InfraRed Telescope Facility (IRTF) is presented, and projections for future analysis are given.

Contents

1	Introduction	6
1.1	Ice Giants: Uranus and Neptune	6
1.2	Atmospheric Observations of ‘Ice Giants’	7
2	Interpretation of Data	9
2.1	Radiative Transfer and Planetary Spectra	9
2.2	Retrieval Theory	13
2.3	NEMESIS Overview	14
2.4	Error Estimates and Retrieval Tuning	17
2.5	Model Efficiency and the Correlated-K Approximation	18
3	Atmospheres of the Ice Giants	22
3.1	Brief Summary of Deep (Tropospheric) Composition	22
3.2	Temperature	24
3.3	Stratospheric Composition	28
3.4	Dynamics	32

Contents	4
3.4.1 Thermal Forcing	32
3.4.2 Zonal Structure	33
3.4.3 Vertical and Meridional Flow	35
3.5 Clouds and Hazes	37
3.5.1 Uranus	37
3.5.2 Neptune	40
3.6 Discrete Features	42
3.6.1 Uranus	43
3.6.2 Neptune	45
3.7 Variability	46
3.7.1 Spatial Variability	47
3.7.2 Temporal Variability	48
4 Results	51
4.1 IRTF Observations	51
4.2 Image Processing	52
4.2.1 SpeXtool	52
4.2.2 Further Data Processing	55
4.2.3 Solar Standards	57
4.3 Preliminary Retrievals	57

5	Future Work	62
5.1	Data Processing	62
5.1.1	Stellar Standard Analysis	62
5.1.2	Air Mass	63
5.2	Choosing a Focused Thesis Topic	64
5.2.1	IRTF Data	64
5.2.2	Other Available Data	65
5.2.3	Improved Methane Absorption Data	66
5.3	Graduate Study Timeline	66

Chapter 1

Introduction

1.1 Ice Giants: Uranus and Neptune

Lying farthest from the Sun, our solar system's ice 'giant' planets, Uranus and Neptune, have been the least understood of the planets ever since man began studying the night sky. While the existence of the classical planets, Mercury, Venus, Mars, Jupiter and Saturn, has been known since ancient times, the first breakthroughs in understanding these planets came from Galileo during the Scientific Revolution. Scientists have studied those five planets avidly ever since Galileo first turned his telescope, which magnified only about thirty times, towards the sky.

Because Uranus and Neptune are much smaller than the 'gas giants' Jupiter and Saturn, and are positioned much farther from the Sun, they appear much less bright than the classical planets. Despite advances in telescopic ability, it was not until 1781 that Uranus was accidentally discovered by William Herschel. The analysis of observed perturbations in Uranus' orbit led astronomers to predict the presence of Neptune, a result confirmed by Johann Gottfried Galle in 1846.

Once discovered, it was possible to determine some basic physical parameters of the ice giants. Uranus and Neptune, are approximately 19 and 30 times farther from the Sun than the Earth, respectively, have the longest planetary orbits in the solar system. Uranus

spends 84 years circumnavigating the Sun, while Neptune completes its orbit in 165 years. The ice giants, like the gas giants, have no rocky surface, and are composed primarily of much lighter material than Earth. Uranus and Neptune are not as large or massive as Jupiter or Saturn, but they are much larger and more massive than Earth. Both have radii about 4 times the size of Earth’s, and masses about 15 and 17 times Earth’s, respectively. These values indicate the densities of Uranus and Neptune are 1.27 and 1.76 grams·cm⁻³ and that they are composed primarily of hydrogen, helium, and various ices, notably water and methane.

Beyond this basic information, largely determined from simple calculations derived from Newtonian orbital dynamics, not much else is known due to the great distances involved in the outer solar system which continue to hamper efforts to study Uranus and Neptune. Telescope observations of these two planets are much less resolved than even those of Jupiter and Saturn. Due to the added cost and time required for spacecraft missions to the outer planets, there are far fewer results from satellite data as compared with the other 6 planets. These challenges are further complicated by an incredibly weak signal in the thermal infrared, as the ice giants’ visible atmospheres are, at best, 50-100 K cooler than their gas giant neighbours. Despite these issues, the limited amount of knowledge attained about the ice giants reveals them to be unique and distinct astronomical bodies.

1.2 Atmospheric Observations of ‘Ice Giants’

To date, only one satellite, NASA’s *Voyager 2*, has visited the ice giants. Flying past Uranus in January 1986, and Neptune in August of 1989, *Voyager 2* gave us our first close look at the ice giants. The *Voyager 2* ice giant visits were both single flybys, and the amount of data collected is limited both in quantity and spatial resolution. Beyond these observations, the only satellite data of the ice giants comes from various Earth-orbital satellites. Hubble Space Telescope (HST) has collected visible, UV, and IR observations of the ice giants, while additional IR observations come from the Infrared Space Observatory (ISO), the Spitzer Space Telescope, and Japan’s AKARI infrared observatory. This data is rounded out by ground-based observations from Earth, though it is only within the past

few years that telescope technology has become advanced enough to resolve individual regions of the ice giants.

The motivation for the research introduced in this paper largely due to the recent acquisition of new telescope data. Some utilises new adaptive optics techniques, which allow more spatially resolved observations to be collected, and hopefully allow some of the fundamental questions surrounding ice giant dynamics and composition to be more successfully addressed.

Chapter 2

Interpretation of Data

This chapter provides an overview of the method with which spectroscopy data will be interpreted to provide information about the ice giants. The first section provides a general, qualitative overview of atmospheric radiative transfer. A more quantitative and thorough discussion on this topic can be found by reviewing the sources of section 2.1 content (Goody and Yung, 1989; Andrews, 2000; Houghton, 2002). Sections 2.2 through 2.5 briefly outline the specific features of retrieval theory and Oxford’s retrieval code that pertain to our proposed analysis. Information in these sections comes primarily from Irwin et al. (2008), Irwin et al. (2009), and Sromovsky et al. (2006).

2.1 Radiative Transfer and Planetary Spectra

The atmospheres of the ice giants have not been directly sampled. We rely therefore upon remote sensing, a technique that determines properties of a planet’s atmosphere from afar, using the electromagnetic spectrum of a planet to offer clues about the chemical and physical structures of the atmosphere. Remote sensing relies on knowledge of how gases and particles in a planet’s atmosphere interact with photons as energy transfers through them. This knowledge allows us to connect the observed spectrum with the physical, thermal, and chemical properties of the atmosphere itself. The aforementioned energy comes either from the Sun in the form of ‘short-wave’ photons ($0.1 - 4 \mu\text{m}$), or from the

thermal energy of the planet itself. When thermally excited electrons return to a lower energy level, they release ‘long-wave’ photons (4 - 100 μm).

The energy levels of a material system at equilibrium temperature, T , will be populated according to the Boltzmann distribution. In a region of sufficiently high temperature in a planetary atmosphere, the frequent molecular collisions between the gases in the air will maintain this distribution. Such an area is said to be in ‘local thermodynamic equilibrium.’ The Planck function, which describes the spectral energy emitted by an ideal, isothermal black body, represents a reasonable approximation of the spectral radiance in such a region.

If the laws of physics are momentarily suspended and it is assumed that no interactions occur between radiation and constituents *within* the atmosphere of a gas giant, then, we would expect to see an atmospheric spectrum comprised of the sum of two Planck functions: one for the long-wave, or thermal emission of the planet’s deep interior, and a second, for the short-wave caused by sunlight incident on the exterior of the planet’s atmosphere and reflected back, as if from a mirror, at the observer. In reality, this is not what we see at all, as photons *do* pass through the atmosphere and interact with the matter along their path.

There are two things that can happen when a photon comes into contact with a planetary atmosphere. If the photon passes through the atmosphere unhindered, ‘transmission’ occurs. If the photon is ‘absorbed’ or ‘scattered’ by the atmosphere, ‘extinction’ occurs. In the thick, observable atmosphere of a giant planet, extinction is much more likely to occur.

As photons of specific, quantised energies strike a gas molecule, they excite the electrons of that molecule to a higher energy level. This results in either ‘scattering’ or ‘absorption.’ Scattering occurs when excitation energy is released as a photon of the same energy, but in a new, random direction. Absorption occurs when the pressure and temperature of the gas environment are sufficiently high to cause a molecular collision to occur before the excitation energy can be emitted. In the latter case, the initial photon effectively converts into microscopic kinetic energy, or thermal energy.

The thermal energy derived from absorption serves to locally heat the atmosphere. The temperature of an atmosphere plays a critical role in determining its spectrum in the long-wave region. A warmer atmosphere has more molecules that carry kinetic energy derived from various rotational and vibrational excitation states of the constituent gases. Sometimes, this kinetic energy is transformed into thermal energy in the form of a quantized, long-wave photon. This energy corresponds to the energy released when the molecule relaxes to a less excited state.

These quantized phenomena do occur, however interactions in which the photons involved do not correspond exactly to the excitation energy of the gas' electrons occur more frequently. These 'continuum reactions' play a critical role in shaping an atmosphere's spectrum.

According to Maxwell's equations, light waves across a broad continuum of frequencies will scatter against the gases and aerosols of the atmosphere. Maxwell's equations, however, provide an overly complex method of describing this scattering given the number of times this will happen across an entire atmospheric observation. Because of this complexity, we simplify the solutions and divide them broadly into three approximations. Geometric scattering occurs when the particle is much larger than the photon's wavelength, and explains rainbows and other large-scale optical phenomena. Rayleigh scattering occurs when the particle is much smaller than the photon's wavelength. Mie scattering applies in the remaining cases, where the particle and wavelength scales are comparable. For a thorough discussion of all these types of scattering, see Goody and Yung (1989).

Continuum absorption processes also play an important role in determining an atmosphere's spectrum. Photons of sufficiently high energy break down molecules through photochemical reactions, known as photo-dissociation or photolysis. These reactions play an important role in atmospheric chemistry on the ice giants. High-energy photons also strip electrons from molecules, resulting in photo-ionization, a process that can be an important source of ions which can serve as condensation nuclei for clouds and hazes in the ice giant atmospheres.

Considering the interactions discussed, it becomes apparent that two idealised Planck functions will be an unrealistic approximation of the atmosphere's spectrum. Gases in

the atmosphere (particularly methane for the ice giants) will strongly absorb photons at certain wavelengths and thermally emit photons at other wavelengths. The gas' column abundance is proportional to its spectral signature. In the short-wave region, gases absorb photons and result in features that drop below a perfect solar spectrum. In the long-wave region, the absorption and subsequent thermal emission of gas molecules will move the true spectrum away from that of an idealised black body. Changes in the long-wave region of giant planets are strongly tied to the atmosphere's thermal profile, which has a local minimum temperature in the middle of the observable atmosphere. In general, gas species below this temperature inversion are evident as absorption features that reduce the planet's emission below the blackbody curve at certain wavelengths. In contrast, gases above the temperature inversion will create emission features that rise above the ideal spectrum. Aerosols have an even more complex impact on the emitted spectrum, absorbing at some wavelengths, and scattering at others. Scattering can be wavelength dependant and vary in direction. Forward scattering moves photons slowly through the atmosphere, while back scattering serves to reflect the majority of the incoming photons in the direction from which they came. Despite these complexities, when the path, temperature, density, atmospheric constituent abundances, and scattering properties of any aerosols are known, the use of a computer model allows a theoretical spectrum for an atmosphere to be computed.

When constructing synthetic spectra based on models of an atmosphere, it is important to keep in mind that none of the absorption or emission features will occur perfectly at one wavelength. The features will instead be 'broadened' by one or more processes that serve to expand the emission feature around the central peak. Lines are broadened 'naturally' since energy levels are not precisely defined. Collision-based 'pressure broadening' occurs when emissions are interrupted by molecular collisions, and become increasingly important at higher pressures and temperatures. Finally, 'Doppler broadening' occurs because molecules are in motion; observer-recorded emission frequencies will be shifted due to the emitting particles' motion. Doppler broadening becomes an important factor at higher altitudes where pressure broadening is weakest. To construct an accurate synthetic spectrum, these three broadening processes must also be considered.

2.2 Retrieval Theory

The process of constructing a spectrum based on a modelled atmospheric structure is known as a ‘forward model.’ The mathematics for this are modelled around the principles outlined in the previous section. Because we have spectral observations at our disposal and desire to understand the structure of an unknown atmosphere, what we need to do is the ‘inverse problem’ or ‘retrieval.’

The retrieval process poses a fundamental problem. Numerical calculations use a discrete set of data points, while we desire a continuous solution; this creates what is known as an ‘ill-posed’ problem. By discretising our solution, some accuracy is lost, but the problem becomes solvable, though still ‘underconstrained,’ as there are more degrees of freedom in the solution than points in the collection of data. The problem is represented by

$$y = Fx + \epsilon \quad (2.1)$$

where y is the measurement vector of m radiances and x is the state vector of n discrete atmospheric descriptions. The values in x might contain temperatures, gas abundances, or aerosol properties at various levels in the atmosphere, though it need not be a complete set of descriptors. F is a matrix operator, which models the physics of the system to translate our complete atmospheric state onto an emission spectrum, and the measurement error covariance matrix is $S_\epsilon = \langle \epsilon \epsilon^T \rangle$

Solving equation (2.1) for an exact solution \hat{x} , the estimate of the atmospheric state vector, or ‘optimal estimator,’ is $\hat{x} = Gy$ which expands to

$$\hat{x} = G(Fx + \epsilon) = Ax + G\epsilon \quad (2.2)$$

where G is the Kalman gain matrix, or retrieval matrix (defined in equation (2.5)). A is an averaging kernel that smooths the final profile, and $G\epsilon$ is the error.

This inverse problem is underconstrained (more elements in state vector than in measurement vector). Solving equation (2.2) directly would result in an infinite set of atmospheric states that would satisfy the noisy measurement vector equally well. It is likely that as

we attempt to resolve the retrieval state vertically, noise in the measurements will become amplified in the retrieved state, creating atmospheric profiles that contain rapid, small-scale oscillations that are physically unrealistic. This problem of attempting to retrieve more vertical information than the measurement error is capable of providing is called “ill-conditioning.” Clearly, an infinite number of solutions that are ill-conditioned (physically unrealistic) are of no use.

To formulate an inverse problem that will yield a single, physically plausible solution, we impose one further condition. The solution must conform to a reference profile of *a priori* measurements, and its associated error covariance matrix, S_α . In addition to providing a single, physically realistic solution, this new constraint helps protect the solution from oversensitivity to experimental error. It also ensures that the solution doesn’t have a microscopic structure generated from numerical calculations which would have been invisible given our original measurement spacing. The new optimal estimator, written in terms of $F = G^{-1}$ rather than G , thus becomes

$$\hat{x} = (S_\alpha^{-1} + F^T S_\epsilon^{-1} F)^{-1} (S_\alpha^{-1} x_\alpha + F^T S_\epsilon^{-1} y) \quad (2.3)$$

with an associated error represented by the estimated total covariance:

$$\hat{S} = (S_\alpha^{-1} + F^T S_\epsilon^{-1} F)^{-1} \quad (2.4)$$

2.3 NEMESIS Overview

NEMESIS (Non-linear optimal Estimator for Multivariate Spectral analysisIS) is the retrieval code that is employed for the research described in this report. The code uses a forward model to generate a synthetic trial spectrum based on the reference profile provided at the outset. The code goes through an iteration process that generates revised and improved trial spectra until a solution is converged upon. Each successive iteration

of the trial spectra is an attempt to minimize the ‘cost’ function

$$\phi = (y_m - y_t)^T S_\epsilon^{-1} (y_m - y_t) + (x_t - x_\alpha)^T S_\alpha^{-1} (x_t - x_\alpha)$$

where y_m is the measured spectrum, y_t is the trial spectrum, S_ϵ is the measurement covariance matrix, x_t is the trial atmosphere’s state vector, x_α is the *a priori* atmosphere’s state vector, and S_α is the *a priori* error covariance matrix.

The specific determination of both covariance matrices should be noted. S_ϵ is formed based on the sum of measurement errors and an estimated forward modelling error. Adding the forward modelling error here is non-standard, but allows the incorporation of any systematic errors associated either with the measurements or with limitations in the computational accuracy directly into the retrievals. As for S_α , since there is not a statistical knowledge of the reliability of the *a priori* state vector, as there is for Earth’s atmosphere, there is not a reliable covariance matrix to input. Instead, NEMESIS forces off-diagonal elements of S_α to decay according to a specified correlation length, l_c , allowing the user to chose an appropriate l_c that vertically smooths the retrieved profiles but does not constrain the retrieval to the *a priori* vector too tightly. NEMESIS sets the off-diagonal values in S_α according to the following formula:

$$S_{ij} = \sqrt{S_{ii}S_{jj}} \exp\left(\frac{-\left|\ln\left(\frac{p_i}{p_j}\right)\right|}{l_c}\right)$$

where p_i and p_j are the i th and j th pressure levels in the *a priori* model. Once off-diagonal elements become sufficiently small, they are set to 0 to allow the code to compute a numerically stable inversion of S_α .

After each iteration, NEMESIS uses the difference between the trial spectrum, y_t , and the measured spectrum, y_m , to compute a new trial state vector, x_{t+1} . Similarly to equation (2.3), but now using the Jacobian, or functional derivative $\frac{\partial F_t}{\partial x}$ to express the sensitivity of the radiance to changes of the state vector, we have

$$\begin{aligned}
x_{t+1} &= (S_\alpha^{-1} + K_t^T S_\epsilon^{-1} K_t)^{-1} [S_\alpha^{-1} x_\alpha + K_t^T S_\epsilon^{-1} (y_m - y_t + K_t x_t)] \\
&= x_\alpha + S_\alpha K_t^T (K_t S_\alpha K_t^T + S_\epsilon)^{-1} (y_m - y_t - K_t (x_\alpha - x_t)) \\
&= x_\alpha + G_t (y_m - y_t) - A_t (x_\alpha - x_t)
\end{aligned}$$

where G_t is the Kalman gain matrix and A_t is the averaging kernel matrix. The Kalman gain matrix is defined as

$$G_t = S_\alpha K_t^T (K_t S_\alpha K_t^T + S_\epsilon)^{-1} \quad (2.5)$$

and A_n is simply equal to $G_n K_n$, again serving as a smoothing term. Note that *a priori* constraints are applied to each iteration of x_t , ensuring that the smoothing imposed by the *a priori* profile is never lost during the iterative process.

In practice, it is possible for K_t to vary considerably between each successive state vector trial solution, which can lead to an unstable series of iterations. In order to prevent this, the actual estimates are calculated by NEMESIS using a slightly modified scheme, based on the Marquardt-Levenberg principle, which includes a breaking parameter to insure that K_t doesn't vary too wildly:

$$x'_{t+1} = x_t + \frac{x_{t+1} - x_t}{1 + a_\lambda}$$

where the initial a_λ is set to 1.0. When an iteration *decreases* the cost function, ϕ , x'_{t+1} replaces x'_t and a_λ is multiplied by 0.3. When ϕ *increases* with a new iteration, that iteration is disregarded (keeping $x_{t+1} = x_t$) and a_λ is multiplied by 10. Though to avoid infinite loops the multiplicative values (0.3 and 10) cannot be factors of each other, the choice is essentially arbitrary.

As each successive iteration calculates a new state vector trial estimate, the estimate is in turn used with the forward model to produce a new trial values for the model spectrum, y , the Jacobian, K , the Kalman gain matrix, G , the smoothing kernel, A , and the cost function, ϕ . The retrieval is considered to have converged when $\Delta\phi < 0.1$, which in turn

means that a_λ tends to 0 and x'_{t+1} tends to x_{t+1} , the optimal estimator. The error of our final optimal estimator takes the form of equation (2.4), but the forward model matrix, F , is now replaced by the Jacobian:

$$\hat{S} = (S_\alpha^{-1} + K^T S_\epsilon^{-1} K)^{-1} \quad (2.6)$$

2.4 Error Estimates and Retrieval Tuning

There are three methods of inputting error into the NEMESIS procedure. Balancing these sources of error is known as ‘tuning’ the model, and must be handled carefully in order to produce sensible and meaningful results and an accurate retrieval error.

S_ϵ is a covariance matrix that is formed from both measurement errors and forward modelling errors. The measurement errors are values derived based on the remote sensing instrument, and is generally either based on the instrument’s noise equivalent radiances, the variance of the data itself, or a combination thereof. The off-diagonal elements of the measurement error are assumed to be 0.

A forward modelling error is used, which is principally a measure of the confidence in our forward model’s accuracy when compared with the real physical principles it is discretising and modelling. Any additional systematic uncertainty discovered in the data can also be accounted for by adding to the forward modelling error.

Finally, S_α is the *a priori* error, which measures the confidence in the *a priori* profile. The modelling of planets for which there are no *in situ* measurements means there is a very poor sense of how accurate the *a priori* model is. Therefore it is much more difficult to confidently set *a priori* error values than it is to set the values in S_ϵ . As a result, tuning the model basically amounts to running the model many times, gradually changing the *a priori* errors until the desired result is reached.

If the *a priori* errors are set too large, the model will operate on the assumption that the *a priori* model is not very good, and the optimal estimator should follow the measurements

much more closely than the *a priori* profile. This produces an under-constrained estimator that follows the measurements closely, but can result in a profile that is physically unrealistic, having huge vertical oscillations. If, however, *a priori* errors are set too small, the model will assume that the *a priori* profile is fairly close to the true profile, and the measurements are unreliable. This results in an over-constrained solution that follows the *a priori* closely, disregarding the measurements. In both cases the retrieval error will generally be unrealistically small (see equation (2.6)).

The “desired result,” then, is one in which *a priori* errors have been set to values which neither over- nor under-constrain the retrieval. Retrieval errors accurately reflect all three sources of error, and the optimal estimator reflects the implications of the measurements with a judicious amount of consideration given to the *a priori* to ensure physical plausibility of the result.

2.5 Model Efficiency and the Correlated-K Approximation

The most computationally intensive part of any retrieval process is running the forward model to produce a model spectrum. When an iterative process that must compute a forward model numerous times is run, it is required that a functional derivative, K , is computed, which causes magnification of the effect of a computationally involved forward model. The most accurate method of constructing the forward model is to use a ‘line-by-line’ method in which every spectral line is handled separately and then convolving over the appropriate instrument function to degrade the model resolution to one that matches the instrument’s resolution. By the time calculations for every absorption line at every required pressure and temperature in your model atmosphere are performed, literally thousands of lines are handled, making the process unsatisfactorily slow for any retrieval process. Band models are often employed, but are not suitable for multiple-scattering atmospheres and will not be discussed. Instead, NEMESIS employs the ‘correlated- κ ’ technique for calculations, further reducing computation time.

Following the technique applied by Lacis and Oinas (1991), the mean transmission of an atmospheric path is

$$\bar{\tau}(m) = \frac{1}{\Delta\nu} \int_{\nu_0}^{\nu_0+\Delta\nu} \exp\left(-m \sum_j \kappa_j(\nu)\right) d\nu \quad (2.7)$$

over a frequency interval ν_0 to $\nu_0+\Delta\nu$, where m is the total absorber column (molecule·cm⁻²). $\kappa_j(\nu)$ is an absorption spectrum expressed in cm²·molecule⁻¹ of the j th line. The sum combines all lines of all absorbing gases. To calculate this function accurately, $d\nu$ would need to be sufficiently small to resolve individual absorption line shapes, and require thousands of calculations. The order of the absorption coefficients has no impact on the overall transmission, and so the equation can be rewritten more efficiently by considering only the fraction of a spectral window over which a particular absorption coefficient lies between κ and $\kappa + d\kappa$:

$$\bar{\tau}(m) = \int_0^\infty f(\kappa) \exp(-\kappa m) d\kappa$$

where $f(\kappa) d\kappa$ is the fraction of the frequency domain for our designated absorption coefficient, and is known as the κ -spectrum. Reordering the absorption coefficients from smallest to largest in the form of

$$g(\kappa) = \int_0^\kappa f(\kappa) d\kappa$$

and noticing that this smooth, increasing, and single-valued function $g(\kappa)$ will have an inverse, $\kappa(g)$, also smooth and single-valued, referred to as the κ -distribution. The transmission can now be expressed as

$$\bar{\tau}(m) = \int_0^1 \exp(\kappa(g) \cdot m) dg$$

or in terms of a numerical integral

$$\bar{\tau}(m) = \sum_{i=1}^N \exp(-\kappa_i \cdot m) \Delta g_i$$

where Δg_i is the weight of the i th quadrature in the summation. The advantage to using this κ -distribution is that it expresses the rapidly varying integral from equation (2.7) as a smooth one. This allows, without much loss of accuracy, for the use of a much larger numerical step size, greatly increasing the speed and efficiency of the forward model calculations.

The κ -tables incorporated into the current version of NEMESIS use a Gaussian quadrature scheme to choose between 10 and 20 quadrature points, finding a balance between sampling accuracy for our κ -distribution and computational efficiency. The mathematics involved in producing a κ -distribution for transmission functions based on absorption coefficients can similarly be used for emission and scattering, helping to increase computational speed in every aspect of the forward model.

Prior to utilizing the correlated- κ method, κ -tables must be produced for any active absorbers present, for all relevant temperatures and pressures given the specific planet in question.

An atmosphere is by nature inhomogeneous, and κ -distributions vary with pressure and temperature, therefore the atmosphere must be split into a series of thin layers that can be considered to be homogenous. K -distributions are calculated for each layer, and conveniently regions of high and low absorption in each layer tend to be correlated well with similar regions in other layers. Given this, once the κ -distribution calculations have been made for each layer, mean properties are computed over the whole atmosphere according to the following formula:

$$\bar{\tau} = \sum_{i=1}^N \exp\left(-\sum_{j=1}^M \kappa_{ij} m_j\right) \Delta g_i$$

where κ_{ij} is a κ -distribution in the i th quadrature point and the j th layer.

In following the correlated- κ method described here, computational time is dramatically reduced by requiring between 10 and 20 distribution calculations, rather than thousands, for each pressure and temperature in the model. Irwin et al. (2008) has found that when comparing correlated- κ results with more accurate line-by-line results, the approximations are accurate within 5%, an acceptable value as uncertainties in gas absorption data and spectral measurements are often of a similar magnitude.

Chapter 3

Atmospheres of the Ice Giants

The ice giants' atmospheres are much colder than their gas giant cousins, and contain a much higher methane and hydrocarbon concentrations. Despite the concentration of these hydrocarbons, largely created through methane photolysis, the observable atmospheres of Uranus and Neptune actually appear to exist in “relative atmospheric purity.” This is due to cold tropopausal temperatures effectively producing a ‘cold trap’ above which many hydrocarbons condense out of the air, leaving a pure He/H₂ mix (Herbert and Sandel, 1999). Though the specific compositional and altitudinal details are still the subject of much debate, it seems that these hydrocarbons condense to form multiple clouds decks in the ice giants' upper atmospheres, with clouds made up of ammonium hydrosulphide (NH₄SH), hydrogen sulphide (H₂S), and methane (CH₄) at various heights. In addition to these large, relatively stable and long-lasting cloud decks, it appears that convection from the ice giants' lower atmospheres often leads to the condensation of methane into localized white clouds, particularly on Neptune (Irwin, 2009).

3.1 Brief Summary of Deep (Tropospheric) Composition

The primary constituents of the solar system's four giant planets are H₂ and He. The most striking differences in composition between the gas giants and ice giants is the specific

ratio of He/H₂, and the higher abundance of methane (CH₄) in ice giants. Tables 3.1 and 3.2 summarize the interior composition of the ice giants.

On the gas giants, helium condenses into droplets within the metallic hydrogen interior, a process which depletes the He/H₂ ratio¹ in the outer layers from the protosolar nebula value of 0.275 (Encrenaz, 2004) to approximately 0.14 – 0.16 (Irwin, 2009). Pressures and temperatures on the ice giants, in contrast, aren't enough to convert the hydrogen into the metallic state, and so in theory the He/H₂ ratio should be higher. Current He/H₂ estimates for Uranus are 0.152 ± 0.033 (Conrath et al., 1987). Conrath et al. (1993) estimates the ratio to be 0.175 for Neptune, while Burgdorf et al. (2003) finds a value of $0.149^{+0.017}_{-0.022}$. Though these estimates are all higher than the values found on the gas giants, they are considerably lower than the protosolar value, though the error bars in Conrath's estimates are just large enough to include the 0.275 value.

There are two distinct spin states of molecular hydrogen, referred to as 'ortho-hydrogen' and 'para-hydrogen.' Given the temperatures ($\gtrsim 300$ K) associated with the deep interiors of the ice giants, these two states are locked in an equilibrium ratio that gives us a para-hydrogen fraction ($f_p = \frac{n_{\text{para-H}_2}}{n_{\text{total H}_2}}$) of 0.25. Moving outward from the deep interior into the troposphere, as the temperature decreases, the equilibrium value of f_p increases (Irwin, 2009). Baines et al. (1995b), Conrath et al. (1998), and Burgdorf et al. (2003) all found mean values for tropospheric f_p on the ice giants to fall quite close to equilibrium².

At the low temperatures and high pressures associated with the ice giants, nearly all of the ice giants' carbon will exist in methane (CH₄). Numerous CH₄ retrievals and models have been performed for Uranus, finding varying volume mixing ratios for the deep atmosphere. Published values are as low as 0.016 and as high as 0.046 (Baines and Bergstrahl, 1986; Lindal et al., 1987; Orton et al., 1987a; Baines et al., 1995b; Sromovsky and Fry, 2007; Irwin et al., 2010). Neptune's deep atmosphere appears to have a comparable CH₄ concentration, with estimates between 0.020 and 0.023 (Tyler et al., 1989; Lindal, 1992;

¹Here and elsewhere in this report, the volume mixing ratio (VMR) will be used when discussing abundance of constituent gases, and $\frac{\text{VMR}_{\text{constituent}}}{\text{VMR}_{\text{all}}}$ when discussing abundance ratios. VMR, also known as a mole fraction, is defined as $\text{VMR} = \frac{n_i}{n_{\text{tot}}} = \frac{p_i}{p_{\text{tot}}}$ for a number of constituent particles, n_i , relative to the bulk atmospheric number of particles, n_{tot} (Andrews, 2000).

²For a more complete discussion of f_p , see section 3.4.3.

Baines and Hammel, 1994; Baines et al., 1995b).

One molecule of particular interest is deuterium (^2H or simply D), an important tracer of evolutionary sequences and timescales in our solar system. In the protosolar nebula, predictions can be made for the D/H ratios both in the spinning centre of hot H_2 , as well as near the icy edges of the disc. Since the formation of the solar system, the former, slightly lower D/H ratio has been slowly reduced in the Sun, where nuclear fusion of deuterium produces ^3He . In most parts of the solar system D/H ratios remain similar to protosolar levels, though in certain locations, often coinciding with material formed from protosolar ices, the slightly higher D/H ratios continue to be enriched through cold-temperature isotope exchange reactions (ion-molecule and molecule-molecule). Thus, provided that current theories are correct, deuterium should be found in the lowest abundance in stars, and the highest abundance in planetary bodies formed farthest from the star and with the highest concentration of protoplanetary and present-day ices. Our solar system's ice giants, therefore, are expected to contain enriched levels of deuterium, which are looked for in the molecules HD and CH_3D (Encrenaz, 2004).

Many observations confirm the prediction that Uranus and Neptune should contain comparatively enriched levels of deuterium. Observations also confirm the prediction that Neptune's level of deuterium enrichment is greater than Uranus' (de Bergh et al., 1986, 1990; Orton et al., 1987a, 1992; Feuchtgruber et al., 1999; Fletcher et al., 2010).

3.2 Temperature

As with any planetary atmosphere of sufficient density, the atmosphere of the ice giants can be divided into two basic regions based on the method of heat transfer. Deep in the atmosphere, where the infrared optical thickness to space is great, heat transfer is most efficiently conducted by convection. As hot air parcels rise, they expand and cool adiabatically, resulting in a mean temperature that cools with increased altitude. This region is named the troposphere. The stratosphere begins above this, once sufficient altitude is reached that the air mass above a parcel of air is thin enough to allow efficient radiative

Table 3.1: Deep Composition of Uranus (updated from Irwin, 2009)

Gas	Mole Fraction	Measurement Technique	Reference
He	0.15 ± 0.033 at $p < 1$ bar	<i>Voyager</i> far-IR	Conrath et al. (1987)
f_p	$0 \leq f_p \leq 0.18$	Visible hydrogen quadrupole	Baines et al. (1995b)
NH ₃	Solar/(100-200) at $p < 10 - 20$ bar	Ground-based microwave	de Pater and Massie (1985)
H ₂ S	$(10-30) \times$ Solar	Ground-based microwave	de Pater et al. (1991)
S/N	$> 5 \times$ Solar	Ground-based microwave	de Pater et al. (1991)
H ₂ O	$\leq 260 \times$ Solar	Thermochemical modelling (to allow 1 ppm CO)	Lodders and Fegley, Jr. (1994)
CH ₄	$0.020 \leq f_{\text{CH}_4} \leq 0.046$	Broadband geometric albedo & H ₂ quadrupole	Baines and Bergstralh (1986)
	0.023 at $p > 1.5$ bar	Radio occultation	Lindal et al. (1987)
	$0.016^{+0.007}_{-0.005}$ at $p > 1.5$ bar	Visible hydrogen quadrupole	Baines et al. (1995b)
	$0.0075 \leq f_{\text{CH}_4} \leq 0.04$	Keck near-IR w/ adaptive optics & HST visible	Sromovsky and Fry (2007)
	0.04 at $p > 1-2$ bar	UKIRT/UIST	Irwin et al. (2010)
CH ₃ D/ CH ₄	$3.6^{+3.6}_{-2.4} \times 10^{-4}$	Ground-based 6,100-6,700 cm ⁻¹	de Bergh et al. (1986)
PH ₃	$< 4 \times$ Solar (2.2×10^{-6}) & no evidence of strong supersaturation	Ground-based 1-1.5 mm	Encrenaz et al. (1996)
	$< 1 \times 10^{-6}$ at $0.1 < p < 3.1$ bar	HST 5 μ m	Encrenaz (2004)
CO	$< 3.0 \times 10^{-8}$	Ground-based 2.6 mm	Marten et al. (1993)
	$< 5 \times 10^{-7}$	Ground-based 1-1.5 mm	Encrenaz et al. (1996)
	$< 2 \times 10^{-8}$ at $0.1 < p < 3.1$ bar	HST 5 μ m	Encrenaz et al. (2004)

Table 3.2: Deep Composition of Neptune (updated from Irwin, 2009)

Gas	Mole Fraction	Measurement Technique	Reference
He	0.19 at $p < 1$ bar	<i>Voyager</i> far-IR	Conrath et al. (1991a)
	0.15 if $\text{VMR}_{\text{N}_2} = 0.3\%$	<i>Voyager</i> far-IR	Conrath et al. (1993)
	$0.149^{+0.017}_{-0.022}$ if $\text{VMR}_{\text{CH}_4} = 2\%$ and $\text{VMR}_{\text{N}_2} < 0.7\%$	ISO SWS/LWS	Burgdorf et al. (2003)
f_p	$0 \leq f_p \leq 0.59$	Visible hydrogen quadrupole	Baines et al. (1995b)
	$f_p \simeq \text{equilibrium} \pm 1.5\%$	ISO	Burgdorf et al. (2003)
NH ₃	Solar/(100-200) at $p < 10 - 20$ bar	Ground-based microwave	de Pater and Massie (1985)
	6×10^{-7} (saturated) at ~ 130 K, 6 bar	Radio occultation	Lindal (1992)
	possibly supersaturated (w.r.t. NH ₄ SH) at $p < 20 - 25$ bar, hence greater than Uranus	Ground-based microwave	de Pater et al. (1991)
H ₂ S	(10-30) \times Solar	Ground-based microwave	de Pater et al. (1991)
S/N	$> 5 \times$ Solar	Ground-based microwave	de Pater et al. (1991)
H ₂ O	$\leq 440 \times$ Solar	Thermochemical modelling (to allow 1 ppm CO)	Lodders and Fegley, Jr. (1994)
	$< 100-200 \times$ Solar	Interior modelling	Podolak and Marley (1991)
CH ₄	> 0.01 at $p > 1.5$ bar	Radio occultation	Tyler et al. (1989)
	0.02 at $p > 1.5$ bar	Radio occultation	Lindal (1992)
	0.022 at $p > 1.5$ bar	Visible reflectance	Baines and Hammel (1994)
	$0.022^{+0.005}_{-0.006}$	Visible hydrogen quadrupole	Baines et al. (1995b)
CH ₃ D/ CH ₄	5×10^{-5}	Ground-based mid-IR	Orton et al. (1987a)
	$6^{+6}_{-4} \times 10^{-4}$	Ground-based 6,100-6,700 cm ⁻¹	de Bergh et al. (1990)
	$(3.6 \pm 0.5) \times 10^{-4}$	Ground-based mid-IR	Orton et al. (1992)
PH ₃	No evidence of strong supersaturation, deep abundance unmeasurable	Ground-based 1-1.5 mm	Encrenaz et al. (1996)
CO	detected in troposphere	Ground-based 1-1.3 mm	Rosenqvist et al. (1992)
	$(1.2 \pm 0.4) \times 10^{-6}$	Ground-based 1 mm	Marten et al. (1993)
	$(0.6-1.5) \times 10^{-6}$ at $0.5 < p < 2$ bar	Ground-based 2.6 mm	Guilloteau et al. (1993)
	$(0.7-1.3) \times 10^{-6}$	Ground-based 0.87 mm	Naylor et al. (1994)
	$< 1 \times 10^{-6}$ (6×10^{-7} preferred)	Ground-based 1-1.5 mm	Encrenaz et al. (1996)
	$(0.6 \pm 0.4) \times 10^{-6}$ (upper troposphere)	Ground-based 1 mm	Hesman et al. (2007)
HCN	none detected	Ground-based 1 mm	Marten et al. (1993)
N ₂	< 0.006 , 0.003 preferred	<i>Voyager</i> far-IR	Conrath et al. (1993)
	< 0.007	ISO SWS/LWS	Burgdorf et al. (2003)

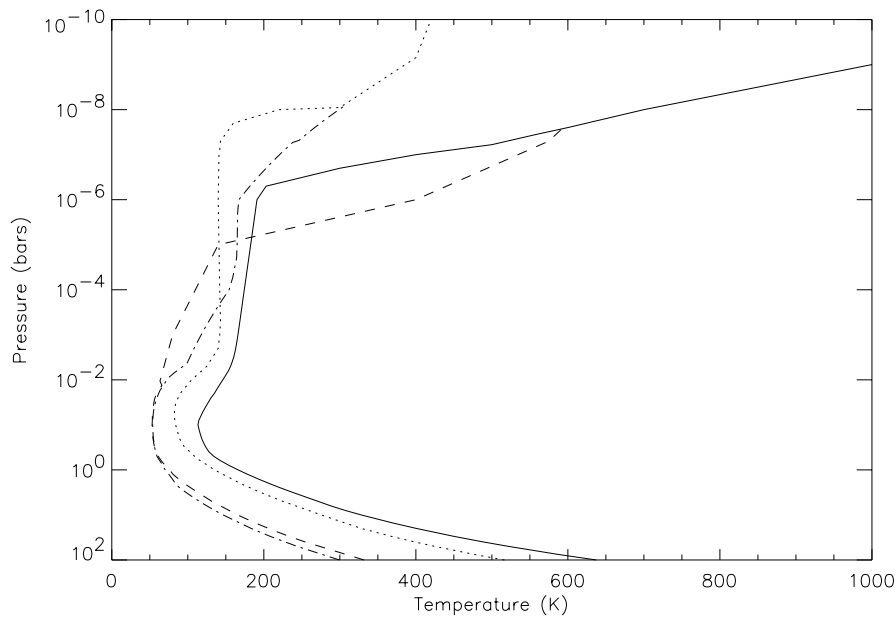


Figure 3.1: Equatorial temperature/pressure profiles of the giant planet atmospheres. Jupiter: solid line, Saturn: dotted line, Uranus: dashed line, Neptune: dot-dashed line. Reproduced from Irwin (2009), used by permission of author.

cooling. The stratosphere is composed of stable, stratified layers. The boundary between these two layers is called the tropopause. On the giant planets, once the tropopause is passed and the stratosphere entered, temperature rises with height due to the high levels of CH_4 absorbing solar radiation from the UV region through the IR.

This research will focus on the observable regions of the upper troposphere and the stratosphere. The relative minimum atmospheric temperature reached at the tropopause is about 50 K on Uranus, and occurs at approximately 100 mbar (Conrath et al., 1991b, 1998). The values for tropopause temperature and height are similar on Neptune (Bishop et al., 1995; Conrath et al., 1998). The ice giant tropopauses are thus some 50 – 100 K cooler than the corresponding regions of the gas giants, as shown in figure 3.1.

The exact nature of the energy balance on the ice giants is poorly understood. Marley and McKay (1999) provide a thorough discussion of the leading theories, and maintain that the stratospheric temperatures of these bodies are regulated primarily by absorption of and emission by ethane (C_2H_6) and acetylene (C_2H_2). There is still much disagreement about the specific nature of the thermal mechanisms in the Uranian stratosphere ($10^{-3} < p < 10^{-1}$ bar), in particular. Most attempts to model this region are unsuccessful at producing

sufficiently high temperatures. Marley and McKay (1999) maintain that methane emission plays the largest role heating this region, while most earlier studies seem to conclude, as in Lindal et al. (1987), that the warmer layers discovered are a result of stratospheric aerosol absorption of solar radiation.

3.3 Stratospheric Composition

Though many abundance profiles exist for trace constituents in Jupiter and Saturn's observable atmosphere, much less is known about trace gases on the icy giants. More difficulty arises on Uranus and Neptune since the thermal radiation is much lower than the gas giants, yielding very poor signal to noise ratios for infrared spectroscopy. In addition, the larger distances involved, and the small number of satellite observations have also limited the quality and quantity of results.

Despite these difficulties, some success has been achieved using IR data from the *Voyager 2* flybys, as well as ISO, HST, *Spitzer*, and AKARI. In the last few years, as telescope data has improved, publications have also begun to provide analysis of ground-based IR observations. In addition to IR spectroscopy, many results have come from various other remote sensing techniques including ground-based microwave, ground-based hydrogen quadrupole, and radio-occultation. Though the specific physics of these non-IR techniques are beyond the scope of this report, the findings will be included in order to paint a better picture of the composition of the ice giant atmospheres. This section outlines the most important information on stratospheric abundances, with complete results to date summarised in tables 3.3 and 3.4.

With so many prominent absorption features and a relatively high abundance, stratospheric methane on the ice giants has been studied quite successfully. Stratospheric levels are generally thought to be quite low, since the ice giant atmospheres are sufficiently cold to trap most hydrocarbons below the tropopause (see section 3.5). Very small stratospheric CH₄ abundances are found on Uranus, with no evidence for values above 10⁻⁵ (Orton et al., 1987a; Yelle et al., 1989; Encrenaz et al., 1998). Stratospheric CH₄ abundances are slightly higher on Neptune, with values on the order of 10⁻⁴ (Orton et al.,

Table 3.3: Stratospheric Composition of Uranus (updated from Irwin, 2009)

Gas	Mole Fraction	Measurement Technique	Reference
H ₂ O	$(6-14) \times 10^{-9}$ at $p < 0.03$ mbar	ISO/SWS	Feuchtgruber et al. (1997)
CH ₄	1×10^{-5}	Ground-based 12 μ m	Orton et al. (1987a)
	$(1-3) \times 10^{-7}$ at $p > 3$ mbar 3×10^{-7} at $3 < p < 5$ mbar	<i>Voyager</i> far-UV	Yelle et al. (1989)
	$(0.3-1) \times 10^{-4}$ at tropopause $< 3 \times 10^{-4}$ at 0.1 mbar	ISO/SWS	Encrenaz et al. (1998)
CO	$< 4.3 \times 10^{-8}$	Ground-based mm	Rosenqvist et al. (1992)
	$< 3.0 \times 10^{-8}$	Ground-based 1 mm	Marten et al. (1993)
	$< 2.7 \times 10^{-8}$	Ground-based 1-3 mm	Cavalié et al. (2008)
HCN	$< 1.0 \times 10^{-10}$ at $0.003 < p < 30$ mbar	Ground-based 1 mm	Marten et al. (1993)
C ₂ H ₆	$< 2 \times 10^{-8}$	Ground-based 12 μ m	Orton et al. (1987a)
	$< 3 \times 10^{-6}$ at 0.1 mbar	Modelled	Encrenaz et al. (1998)
	$< 5 \times 10^{-3}$ at $p < 0.5$ mbar	ISO/SWS	Bézard et al. (2001)
	$\sim 4 \times 10^{-6}$	Ground-based 12 μ m	Hammel et al. (2006)
	$(1.0 \pm 0.1) \times 10^{-8}$ at 0.1 mbar	<i>Spitzer</i> 10-20 μ m	Burgdorf et al. (2006)
C ₂ H ₂	$< 9 \times 10^{-9}$	Ground-based 12 μ m	Orton et al. (1987a)
	10^{-8}	<i>Voyager</i> far-UV	Yelle et al. (1989)
	4×10^{-4} at 0.1 mbar	ISO/SWS	Encrenaz et al. (1998)
	$< 3.6 \times 10^{-3}$ at $p < 0.5$ mbar	ISO/SWS	Bézard et al. (2001)
C ₄ H ₂	$(1.6 \pm 0.2) \times 10^{-10}$ at 0.1 mbar	<i>Spitzer</i> 10-20 μ m	Burgdorf et al. (2006)
CH ₃ C ₂ H	$(2.5 \pm 0.3) \times 10^{-10}$ at 0.1 mbar	<i>Spitzer</i> 10-20 μ m	Burgdorf et al. (2006)
CH ₃	not detected	<i>Spitzer</i> 10-20 μ m	Burgdorf et al. (2006)
	$< 2.8 \times 10^{-3}$ at $p < 0.5$ mbar	ISO/SWS	Bézard et al. (2001)
CO ₂	$(4 \pm 0.5) \times 10^{-11}$ at 0.1 mbar	<i>Spitzer</i> 10-20 μ m	Burgdorf et al. (2006)
	$\leq 3 \times 10^{-10}$	ISO/SWS	Feuchtgruber et al. (1997)

Table 3.4: Stratospheric Composition of Neptune (updated from Irwin, 2009)

Gas	Mole Fraction	Measurement Technique	Reference
H ₂ O	$(1.5-3.5) \times 10^{-9}$ at $p < 0.6$ mbar	ISO	Feuchtgruber et al. (1997)
CH ₄	< 0.02	Ground-based mid-IR	Orton et al. (1987a)
	$7.5^{+18.6}_{-5.6} \times 10^{-4}$	Ground-based mid-IR	Orton et al. (1992)
	3.5×10^{-4}	Visible reflectance	Baines and Hammel (1994)
	9×10^{-4} at 50 mbar 9×10^{-5} at 1 μ bar	AKARI/IRC	Fletcher et al. (2010)
CO	$(6.5 \pm 3.5) \times 10^{-7}$	Ground-based 1-1.3 mm	Rosenqvist et al. (1992)
	$(1.2 \pm 0.36) \times 10^{-6}$	Ground-based 1 mm	Marten et al. (1993)
	2.7×10^{-7} at 30-800 mbar	HST UV reflectance	Courtin et al. (1996)
	$< 1 \times 10^{-6}$ (6×10^{-7} preferred)	Ground-based 1-1.5 mm	Encrenaz et al. (1996)
	$(1.0 \pm 0.2) \times 10^{-6}$	Ground-based 1 mm	Marten et al. (2005)
	0.5×10^{-6} at $p > 20$ mbar 1.0×10^{-6} at $p < 20$ mbar	Ground-based 1 mm	Marten et al. (2005)
	$(0.6 \pm 0.4) \times 10^{-6}$ (lower stratosphere) increasing to $(2.2 \pm 0.5) \times 10^{-6}$ (upper stratosphere)	Ground-based 1mm	Hesman et al. (2007)
HCN	$(3 \pm 1.5) \times 10^{-10}$	Ground-based 1-1.3 mm	Rosenqvist et al. (1992)
	$(1.0 \pm 0.3) \times 10^{-9}$ at 0.003-30 mbar	Ground-based 1 mm	Marten et al. (1993)
	$(3.2 \pm 0.8) \times 10^{-10}$ at 2 mbar; approx. constant w/ height, condenses at 3 mbar	Ground-based 1.1 mm	Lellouch et al. (1994)
	1.5×10^{-9} at $p < 0.3$ mbar, decreasing at lower altitudes	Ground-based 1 mm	Marten et al. (2005)
C ₂ H ₆	$< 6 \times 10^{-6}$	Ground-based 12 μ m	Orton et al. (1987a)
	$(2.5 \pm 0.5) \times 10^{-6}$	<i>Voyager</i> mid-IR	Bézard and Romani (1991)
	$(0.2-1.2) \times 10^{-6}$	Ground-based mid-IR	Orton et al. (1992)
	$< 5.4 \times 10^{-4}$ at $p < 1$ mbar	ISO/SWS	Bézard et al. (2001)
	$(8.5 \pm 2.1) \times 10^{-7}$ at 0.3 mbar	AKARI/IRC	Fletcher et al. (2010)
C ₂ H ₂	$< 9 \times 10^{-7}$	Ground-based 12 μ m	Orton et al. (1987a)
	$6^{+14}_{-4} \times 10^{-8}$	<i>Voyager</i> mid-IR	Bézard and Romani (1991)
	$(0.6-7.1) \times 10^{-8}$	Ground-based mid-IR	Orton et al. (1992)
	$(9-90) \times 10^{-8}$	<i>Voyager</i> IRIS	Conrath et al. (1998)
	$< 5.4 \times 10^{-4}$ at $p < 1$ mbar	ISO/SWS	Bézard et al. (2001)
C ₄ H ₂	$(3 \pm 1) \times 10^{-12}$ at 0.1 mbar	<i>Spitzer</i> 10-20 μ m	Meadows et al. (2008)
C ₂ H ₄	$< 3 \times 10^{-9}$	Ground-based 12 μ m	Orton et al. (1987a)
	$5.0^{+1.8}_{-2.1} \times 10^{-7}$ at 2.8 μ bar	AKARI/IRC	Fletcher et al. (2010)
CH ₃ C ₂ H	$(1.2 \pm 0.1) \times 10^{-10}$ at 0.1 mbar	<i>Spitzer</i> 10-20 μ m	Meadows et al. (2008)
CH ₃	$\sim 3.3 \times 10^{-4}$ at $p < 0.2$ mbar	ISO/SWS	Bézard et al. (2001)
	$< 1.9 \times 10^{-4}$ at $p < 1$ mbar	ISO/SWS	Bézard et al. (2001)

1992; Baines and Hammel, 1994; Fletcher et al., 2010). Fletcher et al. found their values consistent with the theory of a breakdown in the tropopausal cold trap at the south polar region that allows CH_4 to ‘leak’ into the stratosphere.

When small amounts of methane escape the troposphere, they often dissociate when photons bombard them in the thin, high-altitude air. This photolysis, and the resulting molecules and radicals (H_2 , H , CH , CH_2 , and CH_3) serve to enrich the atmosphere with various hydrocarbons which form from products of the photolytic process. Acetylene (C_2H_2) forms readily on both ice giants, and ethane (C_2H_6) forms frequently on Neptune (Encrenaz, 2004).

One stratospheric constituent that has sparked research in recent years is hydrogen cyanide (HCN). This is largely due to the unanswered question of where the molecule’s nitrogen might originate. Rosenqvist et al. (1992) detected HCN mole fractions in the Neptunian stratosphere of $(3 \pm 1.5) \times 10^{-10}$, suggesting that the molecule is produced by reactions between CH_3 and N , the latter supplied by thermal escape from Triton’s atmosphere. Marten et al. (1993) detected higher levels of HCN on Neptune ($(1 \pm 0.3) \times 10^{-9}$ between 0.003 and 30 mbar). They suggested that the particle’s presence could not be fully explained by the small amount of nitrogen escaping from Triton, but rather from upward transport of CO and N_2 from Neptune’s deep interior. The same paper cited an upper limit for HCN in the Uranian stratosphere between 0.003 and 30 mbar of 1.0×10^{-10} . This upper limit was based on lack of internal heat to drive upward convection of required levels of CO and N_2 (see section 3.4.3). Lellouch et al. (1994) detected a HCN abundance of $(3.2 \pm 0.8) \times 10^{-10}$ at 2 mbar on Neptune, stating the abundance should be approximately constant with height until the condensation level at 3 mbar. Marten et al. (2005), however, derived an abundance of 1.5×10^{-9} above 3 mbar, decreasing at lower altitudes. As described, no firm consensus has been reached about the Neptunian abundance profile of HCN, or the origin of the nitrogen required for HCN synthesis.

Oxygen is another molecule that has been the subject of fervent study and speculation in the ice giants’ stratospheres. Stratospheric CO , CO_2 , and H_2O have been detected on both Uranus and Neptune, and the existence of these molecules raises the question of where the oxygen, necessary for their production, comes from. Most H_2O in the ice giants

should be trapped below the cold tropopause, so most of the stratospheric H₂O must come from external sources. CO₂ can be formed by either using externally derived oxygen or from stratospheric reactions between H₂O and CH₃. External sources for oxygen could be small meteoroids, silicate dust particles, or simply an interplanetary flux of water ice from the rings and satellites of the ice giants. It is estimated that approximately 10⁵-10⁶ molecules·cm⁻²·s⁻¹ of H₂O is imported from these sources to the gas giants' atmospheres. Most recent studies, however, favour a combination of both internal and external oxygen sources. There seems to be no consensus reached in the literature to date, as examples can be found of papers that conclude oxygen must be derived from every possible combination of internal and external sources (Rosenqvist et al., 1992; Marten et al., 1993; Courtin et al., 1996; Feuchtgruber et al., 1997; Encrenaz, 2004; Encrenaz et al., 2004; Hesman et al., 2007; Fletcher et al., 2010).

3.4 Dynamics

The atmospheric dynamics of the ice giants are probably those least understood in our solar system. The information that is known raises some fascinating questions.

3.4.1 Thermal Forcing

The dynamics of any planetary atmosphere are driven by a combination of solar and internal heating. Analysis of the *Voyager 2* data from the 1986 Uranus flyby revealed a planet with a miniscule internal heat flux, representing no more than 6% of the planet's total heat flux (Marley and McKay, 1999). This fact, combined with Uranus' 98° axial tilt, makes it a unique case in atmospheric forcing among the planets of our solar system. During the *Voyager 2* flyby, Uranus was near its northern winter solstice, therefore the planet's extreme obliquity meant the southern hemisphere was receiving nearly all of the planet's solar heat flux. Given the nearly constant solar forcing across the planet during the 10 or 15 years leading up to the flyby, the dynamics and atmospheric circulation of Uranus seemed, at the time, to be rather uninteresting and static. The only major

surprise was that the heat absorbed by the southern hemisphere seemed to be fairly efficiently distributed across the planet through some form of meridional transport (Flasar et al., 1987). Another major motivation for the research introduced here is that Uranus moved through its northern vernal equinox in 2007. Preliminary data (Irwin et al., 2009; Norwood and Chanover, 2009; Sromovsky et al., 2009; Irwin et al., 2010) suggests that the rapid change in solar forcing produced a dramatic increase in the atmosphere's dynamic complexity. Despite Uranus' great distance from the Sun, it seems that its atmospheric dynamics are driven almost totally by solar contributions; this recent data of Uranus represents a unique opportunity to observe the planet during a time of relatively quick changes in thermal forcing. Similar opportunities will not occur again until nearly 2050.

Neptune's thermal forcing, though different than Uranus', also offers a fascinating and unique set of questions. While Uranus' emitted versus absorbed heat flux (1.06) is considerably lower than that of the gas giants (~ 1.7), Neptune's heat flux ratio of 2.52 is far greater. Despite its distance from the Sun and being as cold as Uranus, Neptune appears to have an incredibly powerful internal heat source, a poorly understood characteristic. The dynamics of the planet, are primarily internally driven, with solar contributions playing a lesser role than in the other three giant planets. Despite the largely internal thermal forcing on the planet, brightening of the methane and ethane emissions in the south polar region, coincident with the 2005 southern summer solstice, supports possible solar forcing as well (Hammel et al., 2007). Increased resolution of telescopic data may provide insights into the nature of these dynamics as well as the nature of this internal heat source.

3.4.2 Zonal Structure

Though Uranus and Neptune do not have the same striking visible belt structure of the gas giants, thermal sounding and observation of cloud velocities indicate that they, like their larger neighbours, have a latitudinally-dependant zonal wind structure. The specific characteristics of Uranus' and Neptune's zonal wind structures, however, are as different as possible from the gas giants.'

Unlike the gas giants, which have a long series of narrow, latitudinal belts and zones,

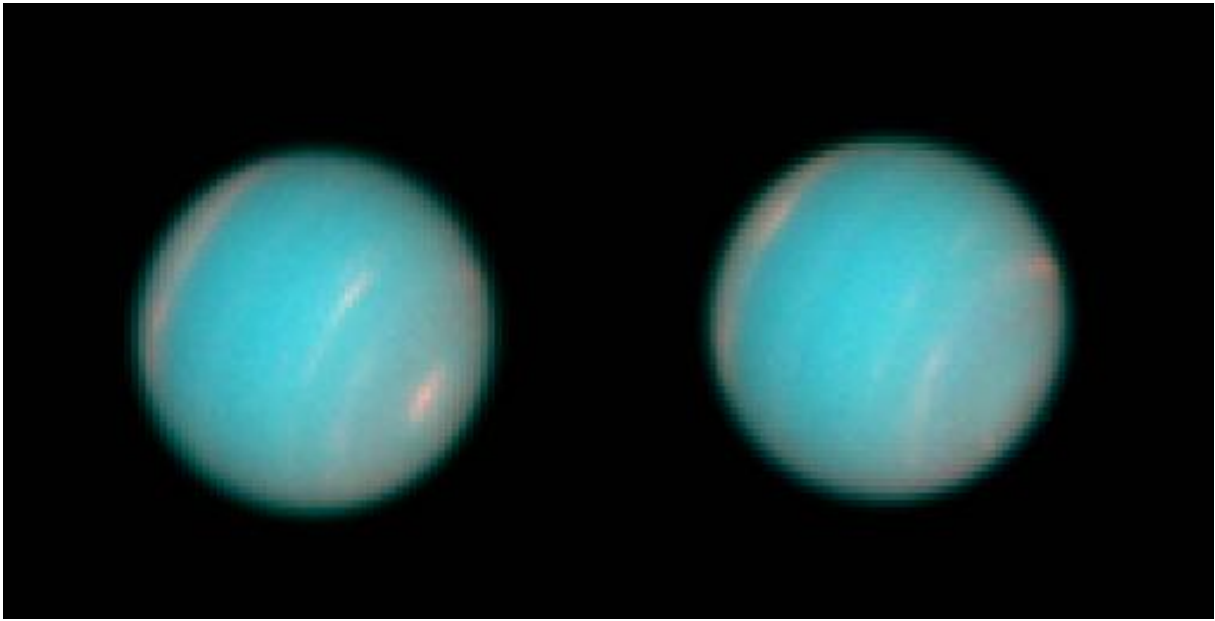


Figure 3.2: HST image of Neptune shows clear zonal structure of planet. Photo courtesy NASA/JPL.

Uranus and Neptune both seem to have one main equatorial jet, and a single pair of mid-latitude jets each (see figure 3.2). The equatorial jets of the ice giants, in contrast to those found on Jupiter and Saturn, are retrograde in direction, while the mid-latitude jets are prograde (Lindal et al., 1987; Sromovsky et al., 2009). Excepting the strong equatorial jet found on Saturn, the mid-latitude jets on Uranus and Neptune are much stronger than any jets found on Jupiter and Saturn, with wind speeds reaching above 200 m/s. Uranus' equatorial jet is smaller, with winds of less than 100 m/s, a figure very comparable with most zonal wind speeds of the gas giants. Neptune's equatorial jet displays wind speeds of approximately 400 m/s, making it and Saturn's equatorial belt home to the outer planets' fastest zonal wind speeds (Irwin, 2009). A slight asymmetry of the northern and southern prograde jets is apparent on Uranus, and it has been suggested that this is a permanent pattern rather than a seasonally reversing phenomenon, though it is not a well-understood attribute (Sromovsky and Fry, 2005; Sromovsky et al., 2009). A comparative plot of zonal wind speeds of all giant planets is included in figure 3.3.

Though the full dynamics and intricacies of the zonal wind structure on the ice giants are not fully understood, a recent simulation has provided the first major success at modelling the zonal structure of the ice giants. Lian and Showman (2010) present a model with 3

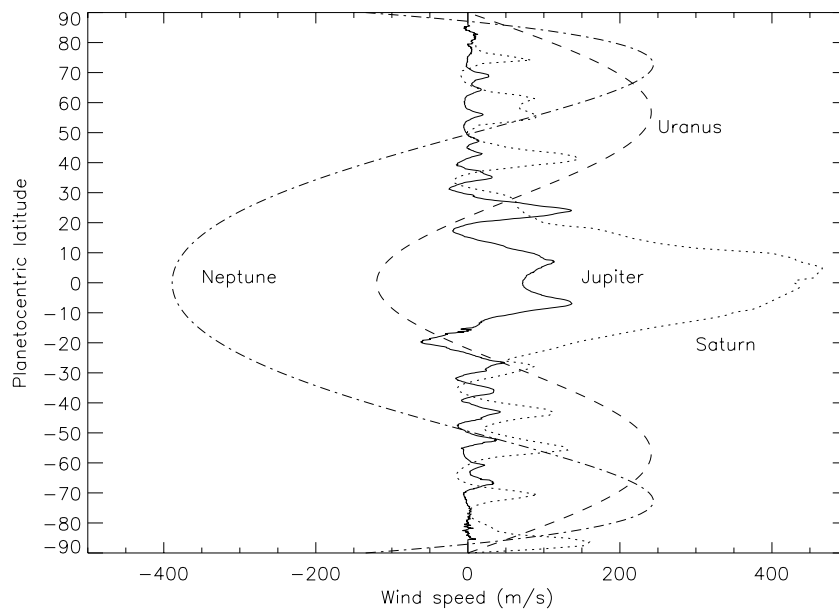


Figure 3.3: Zonal wind structure of the giant planets. Solid line: Jupiter, dotted line: Saturn, dashed line: Uranus, dot-dashed: Neptune. Reproduced from Irwin (2009), used by permission of author.

major zonal jets. Equatorial jets are in the retrograde direction, as observed on both Uranus and Neptune. Their model is a 3-dimensional numerical simulation driven by large-scale latent heating from condensation of water vapour. In general, they found that stable zonal structures are dependant on the rotation rate and radius of the planet. When setting water vapour levels at approximately 30 times the solar abundance on both ice giants, however, they find the equatorial jet becomes retrograde regardless of planet size and rotation rate.

3.4.3 Vertical and Meridional Flow

The conversion between ortho- and para- H_2 requires the molecule to change its spin, so another molecule (in a giant planet, this molecule is typically an aerosol) must act as a catalyst for the conversion. In the deep atmosphere, the para- H_2 fraction, f_p , reaches a high-temperature equilibrium ratio of $f_p = 0.25$. An effective means of determining vertical and meridional flow in the giant planet atmospheres is to retrieve distributions of stratospheric f_p . This retrieved distribution can be used as a tracer of the amount of

upwelling from the deep interior, as well as of the abundance of catalytic aerosols (Massie and Hunten, 1982; Fouchet et al., 2003).

Because there is an abundant amount of aerosols present at the 1 and 10 mbar levels on Uranus (Pollack et al., 1987) and the stratospheric values of f_p are close to equilibrium (Conrath et al., 1998; Fouchet et al., 2003), it can be assumed that there is little upwelling occurring in the Uranian atmosphere, based on these two sets of observations. The slight latitudinal variations evident in f_p show that values are lower in the southern hemisphere (closer to deep equilibrium) and higher in the north. This implies that more upwelling occurs in the southern hemisphere. The hemisphere's position during the observed solstice indicate that upwelling (and associated subsidence in the northern latitudes) is a probable means of heat transport from the sunnier, warmer southern hemisphere into the northern. This northward transport of warm material is also supported by the observation of an equatorial opacity feature associated with an influx of ring material that shifts northwards by 1-2° at lower altitudes (Karkoschka and Tomasko, 2009). Current levels of latitudinal f_p variation on Uranus, having just passed the northern vernal equinox, will be quite interesting as they may imply annual changes in this observed heat transport on Uranus.

Neptune has higher-than-predicted tropospheric cloud layers and more dynamic and spatially varied stratospheric hazes (see section 3.5.2). These support a more active vertical and meridional transport system (Baines et al., 1995a,b). Though the hazes are optically thicker than those on Uranus, the actual number of catalytic particles is probably smaller, as the particles themselves are larger (Pryor et al., 1992). This implies less efficient catalysis of the ortho-/para-H₂ conversions, and explains the larger differences between observed stratospheric levels and the deep equilibrium of f_p . In the stratosphere, f_p values are lowest at midlatitudes, which correspond to the coolest stratospheric temperatures on Neptune. This also validates the model that midlatitudes are the regions of most rapid upwelling from the cold interior.

3.5 Clouds and Hazes

An important characteristic of the ice giants is their thick cloud features, generated as gaseous molecules condense in their cold atmospheres. Simple models of these clouds, known as Equilibrium Cloud Condensation Models (ECCM) predict that warm gas parcels from the interior rise, unmixed with the surrounding air that is increasingly cooler, until it reaches an altitude where its VMR is equal to the saturation VMR of the surrounding air. At this point, assuming the existence of solid particles that can serve as cloud condensing nuclei, the gas in the rising parcel begins to condense and form clouds. As the parcel continues to rise into cooler air, it leaves the condensed cloud particles behind. The mixing ratio of the gas essentially follows the decreasing saturated VMR with altitude. Once the gas parcel reaches the tropopause, where the temperature begins to rise again, the saturated VMR also rises. The VMR of the gas essentially remains constant above the tropopause, however, because of the cloud particles left behind at lower altitudes. The tropopause serves as an effective “cold trap” that keeps most condensable gases trapped below, in the troposphere. This considerably limits the abundances that can be reached in the stratosphere.

This model makes some very inaccurate assumptions, including that the rising air parcel does not mix, horizontally or vertically, with the surrounding air. The ECCM thus provides accurate predictions for the base of cloud layers, but does not accurately predict abundance profiles above the cloud bases, nor the optical or vertical thickness of the clouds. These latter two features are dependant on the rate of uplift, which governs how much mixing can be achieved with the surrounding air, and controls the size and rate of formation of cloud aerosols. Aerosol size, in turn, dictates how these particles move in the atmosphere, and at what speed they are able to descend to warmer temperatures and re-evaporate.

3.5.1 Uranus

This simple ECCM predicts that a large water cloud would exist between 100 and 1000 bar for Uranus, depending on the exact H₂O abundance in the deep atmosphere. Above

this, at approximately 40 bar, an ammonium hydrosulphide (NH_4SH) cloud is expected to form. This will be followed by a cloud of either ammonia (NH_3) or hydrogen sulphide (H_2S) somewhere between about 2 and 8 bar, depending on which of those species has a higher deep abundance³. Finally, at about 1.5 bar, a methane (CH_4) cloud⁴ is predicted (Irwin, 2009).

Though remote sounding cannot be used to detect the deeper decks of predicted clouds on Uranus, several of the upper layers of clouds have been observed. *Voyager 2* detected two cloud decks, an optically thin deck located at about 1.2-1.3 bar, and an optically thick cloud located at approximately 2.7-3.1 bar. The upper cloud is apparently the predicted methane cloud, as the methane mole fraction appears to rapidly decrease above this level. The optical thinness of the cloud is explained either by a thin vertical extent, by rapid condensation to large particles that rain out of the cloud quickly, or by a combination of these factors (West et al., 1991). The deeper cloud, though no spectral identification was made, is probably the top of a “UV-irradiated H_2S ice” cloud (Baines and Bergstralh, 1986). Baines et al. (1995b) and Encrenaz (2004) detected an “optically thick cloudtop,” corresponding to the predicted NH_3 or H_2S cloud, at 3.1 bar.

Several other recent Uranus studies have also produced evidence for an upper, optically thin methane cloud, and a deeper, optically thick cloud consistent with H_2S ice. These conclusions, however, are not undisputed. Sromovsky et al. (2006), using refined temperature dependence parameterizations for their band model, detected two similar cloud layers at 2 and 6 bars. Irwin et al. (2007, 2009, 2010) also support the 2-cloud hypothesis, describing a cloud at 1-2 bar running from 50° S to 45° N, with increased thickness at the 45° S circumpolar collar (see section 3.6) and a deep cloud at 8-10 bar, thickest at the equator and thinning towards the poles. Sromovsky and Fry (2007, 2008), in contrast, found no evidence of scattering at 1.2 bars (the predicted level of the methane cloud). Instead they suggest two H_2S clouds, one at 2-3 bar, and another at 6-8 bar in which atmospheric sulphur is enriched compared to carbon. This proposed deep cloud layer has

³Since the two species in question react together to form NH_4SH , the lesser of the two will be consumed in the production of the deeper NH_4SH cloud.

⁴Signorell and Jetzki (2007) predict that any methane clouds on the ice giants will contain crystalline ices.

very low absorption, indicating either a cloud contaminated by an absorbing haze, or a very thin vertical extent.

Above the cold trap at the tropopause, most condensable material in the Uranian atmosphere is well below the saturated VMR and does not form cloud layers. Despite this, there is abundant evidence in the stratosphere, where incident solar radiation plays a large role in the atmospheric chemistry of the planet, for a number of haze layers formed from the molecular products of methane photolysis. Moving upwards from the tropopause, the ECCM predicts a C_2H_6 ice layer below 15 mbar, a C_2H_2 ice layer below 2.5 mbar, and a C_2H_4 ice layer below 0.1 mbar for Uranus. Primary stratospheric hazes are thought to be C_2H_6 , C_2H_2 , C_4H_2 , C_2H_4 , and other polyacetylenes ($C_{2n}H_2$ for $n = 2, 3, 4, \dots$). These hazes combine to produce an optically thin stratospheric layer, lying mostly between the tropopause and the 1 mbar level (Irwin, 2009).

The observed particles in this haze seem to have approximate radii of $0.1 \mu\text{m}$, and act as absorbers of solar radiation. They also scatter incident light, producing a total optical depth of between 0.4 and 1.0. Unlike the stratospheric hazes observed on Jupiter and Saturn, the hazes in the Uranian stratosphere appear to darken considerably towards the poles at wavelengths below $0.35 \mu\text{m}$ (Baines and Bergstralh, 1986; West et al., 1991; Irwin, 2009). Baines and Bergstralh (1986) characterized these ice particles with an upper limit of $0.1 \mu\text{m}$ in radius, suggesting the particles gradually coalesce and sediment out of the atmosphere below 30 mbar. Pollack et al. (1987) determined two other haze characterizations consistent with their data. At 44 mbar, an ice particle number density of $100\text{-}300 \text{ particles}\cdot\text{cm}^{-3}$ given radii between 0.078 and $0.091 \mu\text{m}$ produced agreement with data, as did $1\text{-}3 \text{ particles}\cdot\text{cm}^{-3}$ for particle radii of $0.13 \pm 0.02 \mu\text{m}$. The paper preferred the latter solution, given its more probable particle density.

Finally, in contrast to the majority of available published data, Karkoschka and Tomasko (2009) suggest that their HST dataset of Uranus was modelled more accurately using an extended stratospheric haze layer, rather than the typically assumed cloud condensation models. They suggest that most of the haze is produced near 1.2 bar and slowly drops through the atmosphere to about 2 bar before thinning. They admit, however, that “both kinds of models are observationally difficult to distinguish.” They base much of the

paper's analysis on the more typical discrete cloud model, justifying their decision because adding extended cloud layers "would have only added free parameters without significantly changing results." The paper also suggests the hazes to be conservatively scattering, given observed dark albedos in near-IR methane windows. Strongest UV absorption is reported in the high southern latitudes.

3.5.2 Neptune

The ECCM model predicts the same series of tropospheric cloud decks on Neptune to those predicted on Uranus, differing only slightly in the predicted altitudes. The large water cloud is predicted at more than 50 bar, and is presumed even larger than the H₂O cloud on Uranus, as the abundance of deep oxygen on Neptune is so great. The NH₄SH cloud is predicted at 37-50 bar, the H₂S/NH₃ cloud at 7-8 bar (again the specific species is dependant on which has a higher tropospheric VMR), and finally the CH₄ cloud⁵ at 1.5-2 bar (Baines et al., 1995a; Irwin, 2009).

Again, most observations, though not perfectly equivalent, indicate that the ECCM has produced a reasonable model. As with Uranus, the top two cloud layers have been directly observed, with various conclusions about their specific properties and altitudes. Baines and Hammel (1994) report an opaque cloud at 3 bar, which most likely corresponds to the predicted H₂S/NH₃ cloud. Baines et al. (1995a,b) revise the previously reported, deep cloud altitude to 3.8 bar, and describe a methane cloud at 1.5 bar. The deep cloud is consistent with pure H₂S, implying a lower than predicted VMR for NH₃, and a S/N ratio highly enriched compared to the solar ratio. The optical depth, well above the predicted condensation level of 7-8 bar, indicates a high degree of vertical mixing (see section 3.4.3). The methane cloud is optically thinner than in models, implying quick rates of condensation and rain out. Atreya et al. (2006) propose a deep water-ammonia ionic ocean that might account for lower-than-predicted ammonia mole fractions in the region of the condensed clouds.

⁵Again, Signorell and Jetzki (2007) predict crystalline ices in any ice giant methane clouds.

As with Uranus, a number of different stratospheric haze layers, composed with molecular products of methane photodissociation, are predicted. Neptune's more active transport dynamics cause more haze-producing methane to reach the stratosphere and produces hazes more spatially varied and dynamic than the Uranian counterparts. It is proposed that rapid growth of CH₄ particles rain out quickly, keeping methane cloud decks thin. As a result, stratospheric hazes have comparable optical thicknesses to that of the CH₄ cloud layer. Principle components of this stratospheric haze are C₄H₂, freezing below 2 mbar, C₂H₂ below 6 mbar, and C₂H₆, condensing below 10 mbar. It is possible that a second, stratospheric CH₄ haze layer exists at a stratospheric condensation level (Baines et al., 1995a,b; Irwin, 2009).

Observed stratospheric haze particles are characterized by 0.2 μm radii between 5 and 100 mbar. The particles have an optical depth of 0.19 ± 0.08 and a radius of 0.20 ± 0.05 μm for incident light at 265 nm. For light at 750 nm, the particles have an optical depth of 0.05 ± 0.02 and a radius of $0.25^{+0.15}_{-0.25}$ μm (Pryor et al., 1992; Baines et al., 1995b). According to one study, mass column abundance of the haze is no greater than 0.61 μg/cm², while column density is approximately 10⁶ cm⁻² in another study (Baines and Hammel, 1994; Gibbard et al., 2002). Haze opacity is less than 0.075 at 619 nm and 0.042 at 890 nm (Gibbard et al., 2002). It is estimated that between 6 and 14% of UV and visible light is absorbed by the stratospheric haze. This absorption rate may explain why temperatures in Neptune's lower stratosphere are 40 K warmer than expected. Other contributing factors could be tidal heating from Triton or the breaking of vertical gravity waves from the active troposphere (Pryor et al., 1992; Baines et al., 1995b).

Some interesting evidence suggests that these extended Neptunian haze layers extend down into the troposphere, rather than being replaced by optically thick, vertically thin cloud decks. Baines and Hammel (1994) detect an extended tropospheric CH₄ haze layer of column abundance bounded at 11.0 μg/cm² with an opacity bounded above at 0.104 at 619 nm and 0.065 at 890 nm. Particle size for a tropospheric haze is suggested to be 15-40 μm in one study (Burgdorf et al., 2003), while another suggests smaller particles with 0.2 μm radii and a column density between 10⁷ and 10⁹ cm⁻² for pressures above 0.6 bar (Gibbard et al., 2002). Max et al. (2003) highlight data consistent with an extended

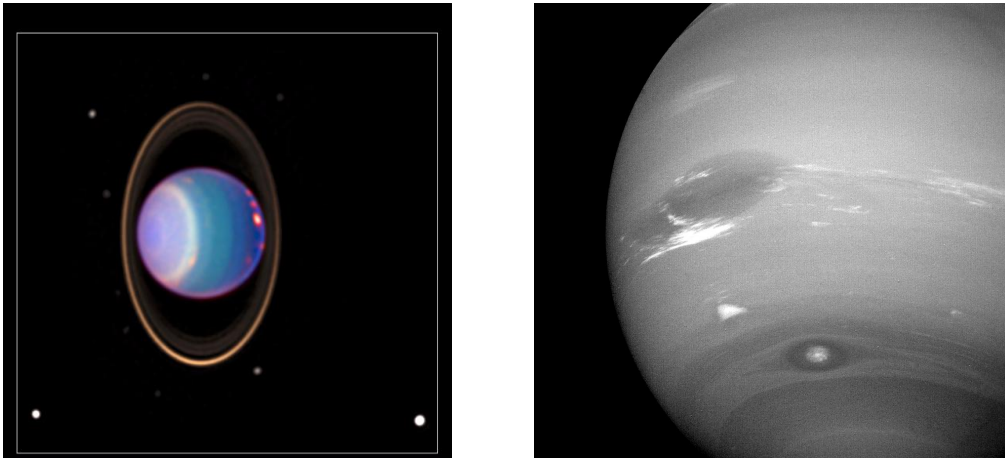


Figure 3.4: Left frame: False color 1998 HST image of Uranus. Many discrete cloud features are visible. Right frame: *Voyager 2* image of Neptune. GDS of the *Voyager* flyby as well as several other discrete cloud and storm features in the southern hemisphere are visible. Photos courtesy NASA/JPL.

haze layer somewhere between 0.1 and 3 bar. They are, however, unable to characterize at what specific altitudes this haze is evident, and suggest that it may be nonexistent in some regions of the planet. Pryor et al. (1992) detect an extended haze in the troposphere, stating that if it exists, the CH_4 cloud deck predicted at 2 bar would be limited to an optical depth of 0.8, while the haze itself would be limited to an optical depth of 0.1 at 750 nm. Clearly, disagreement about a possible extended haze in the troposphere remains, and a range of characteristics have been proposed, with no single hypothesis gaining favour.

3.6 Discrete Features

When it comes to local phenomena and meteorology, the ice giants offer some of the most extreme examples in the solar system (figure 3.4), and the striking contrasts between the two planets becomes most evident. Uranus, for example, has the lowest eddy diffusion coefficient of the giant planets, while Neptune (along with Saturn) has the highest (Encrenaz, 2004).

In addition to the large, global-scale cloud decks and hazes discussed in the previous section, evidence supports the existence of many discrete features visible from above on

both ice giants. Numerous papers detail observations of discrete cloud features interpreted to be convective methane clouds similar in structure and formation to cumulus clouds on Earth.

Though convective clouds do exist on Uranus, they tend to occur less frequently and appear less bright, due to the low stratospheric methane of the planet and its generally calm interior. In most cases, it is believed the Uranian convection clouds do not penetrate the cold trap at the tropopause (Karkoschka, 1998; Hammel et al., 2005b,a; Sromovsky et al., 2007). Conversely, on Neptune where more methane is present and more tropospheric turbulence is found, the convective clouds are more noticeable, particularly in the midlatitudes. A large amount of data has been accumulated in the last decade, both from ground-based telescopes with adaptive optics and from orbital observatories, that describes and analyzes discrete features on both planets. The years surrounding the Uranian equinox in 2007 have shown a dramatic increase in the number of observations and led to a large set of data detailing discrete objects on Uranus. The most notable ice giant features are described in sections 3.6.1 and 3.6.2, and the less notable features found in tables 3.5 and 3.6.

3.6.1 Uranus

The long-lived Uranian cloud, named S34, exhibits an approximately 1000-day oscillation between 32 and 36.5° S. A rapid oscillation of a 0.57° amplitude and approximately 31-day period is superimposed over the major oscillation. S34 varies its longitudinal drift between -20 and $-31^\circ/\text{day}$, and is visible due to unusual particles in the atmosphere near 700 mbar and 4.5 bar, possibly the result of a non-barotropic Rossby wave (Sromovsky and Fry, 2005, 2007).

In 2006, Uranus was observed to have a “Dark Spot” similar to the famous Great Dark Spot (GDS or NGDS-31) on Neptune. Located at 28° N, the Uranus Dark Spot appears 5° wide, 2° tall, and circles the planet approximately 20 m/s faster than bright features located at the same latitude (Hammel et al., 2009).

Table 3.5: Summary of Observations of Discrete Features on Uranus

<i>Observation Dates</i>	<i>Observation Notes</i>	<i>Reference</i>
1996-1998	increased convective activity	Sromovsky et al. (2001)
1997	HST images claim 10 times better contrast than previous best near-IR results	Karkoschka (1998)
1999	increased cloud activity compared to <i>Voyager</i>	Max et al. (2003)
	most cloud tops remain below tropopause	
2000	8 small cloud features observed above methane cloud deck ($0.5 < p < 1$ bar) with 1500 ± 500 km diameters	De Pater et al. (2002)
2000, 2002	cloud tops reach lower stratosphere (northern latitudes)	Gibbard et al. (2003)
	cloud tops reach tropopause (southern latitudes)	
2002	opacity spike spanning 0.2° centered at equator, believed to be caused by influx of ring particulate	Karkoschka and Tomasko (2009)
2003, 2004	70 cloud features observed with timescales ranging from hours to years	Sromovsky and Fry (2005)
2004	feature observed at 26° N and 200 mbar is 11 times brighter than background (strong counterexample to trend of troposphere-restricted meteorology)	Sromovsky and Fry (2007)
2007	28 cloud features observed	Sromovsky et al. (2009)
	several long-lived features grouped at 30° S but drift northwards from June to September	
	several long-lived features grouped at 30° N and remain at fixed latitude but slowly begin to look like GDS with companion light features	

The brightest feature observed in the Uranian atmosphere as it approached equinox (also the brightest observed to date) is described by Sromovsky et al. (2007). This feature existed at 30.2° N from at least November of 2004 to October of 2005, and like S34 has two oscillatory modes superimposed over each other. Observations were too brief to fully characterize the slow oscillation, and the possibility of a period as long as 753 days cannot be eliminated, it is believed that this slow oscillation has a period of about 448 days. This oscillation is in the latitudinal direction, has an amplitude of approximately $0.6\text{-}0.7^\circ$, and is possibly associated with a Rossby wave. The faster oscillation, suggested to be inertial, has an amplitude of 1.2° of latitude and a suggested period of 0.68455 days. This feature brightness is derived from cloud particles lofted from 400-500 mbar up to 300 mbar, increasing the effective cloud fraction by a factor of 5.

Another feature of note on Uranus is the “Bright Band,” or “Circumpolar Collar” located at 45° S, which circles the planet. Sromovsky and Fry (2007) propose that the collar is produced by greater particulate scattering in the troposphere near 2 bar. Irwin et al. (2007) explains variation in the bands’ brightness at different wavelengths to be latitudinal changes in the structure of the cloud.

The wide array of meteorological features present provide evidence that the initial *Voyager 2* impression of Uranus as a bland and uninteresting body is far from accurate. In addition to the large number of interesting features observed, their rate of change around the time of the 2007 northern vernal equinox (see section 3.7.2) is quite striking.

3.6.2 Neptune

Though farther away and harder to resolve spatially, studies of discrete phenomena on Neptune have also benefited from the past decade’s advances in telescopic ability.

Two GDS features have been observed repeatedly in Neptune’s northern hemisphere, and are described by Sromovsky et al. (2001, 2002). NGDS-31, a dark spot at $31\text{-}32^\circ$ N was identified after the *Voyager 2* flyby. Several smaller features that are located around it match its circumnavigational speed, rather than moving at the rate of the mean zonal

Table 3.6: Summary of Observations of Discrete Features on Neptune

<i>Observation Dates</i>	<i>Observation Notes</i>	<i>Reference</i>
1989-2000	southern GDS drifted equatorward, disappearing in 1990	Sromovsky et al. (2002)
1996	band of nonaxisymmetric features centred at $60 \pm 2.5^\circ$ S with heights between 60 and 230 mbar	Sromovsky et al. (2001)
1996, 1997	resolved storm features with radii ≥ 1500 km	Gibbard et al. (2002)
1999	resolves cloud features to 1000 km using adaptive optics system on Keck II	Max et al. (2003)
2000, 2002	stratospheric features, probably due to subsidence of stratospheric haze, identified from 30° N to 45° S between 23 and 64 mbar	(Gibbard et al., 2003)
	tropospheric features, probably due to upwelling and condensing methane, identified from 30° S to 50° S between 0.10 and 0.14 bar	
	tropospheric features identified, probably due to discrete upwelling regions in general subsidence zones, at 70° S between 0.17 and 0.27 bar	

flow. NGDS-15 is a unique GDS, having the lowest latitude of any observed, as well as existing atypically free of companion objects. Both features have been observed frequently enough to note relatively stable drift rates, both latitudinally and longitudinally. This stability contradicts current results of GDS numerical models. Hypothetical explanations for this disagreement are the existence of unresolved latitudinal structure in the zonal wind background or unknown nuances in the vertical stability.

3.7 Variability

Voyager 2 observations classed Uranus as a planet with little spatial variability and a lack of many (or any) exceptional features, and Neptune as a far more “interesting” planet that had some of the most rapidly changing weather and features, spatially and temporally, in the solar system. Ironically, it has been Uranus for which more study of variability has been possible. Measuring anything more resolved than disc averages wasn’t possible on the ice giants until the past decade or so, making studies of variability on the planets quite

limited. As more Earth-orbital telescopes were launched and adaptive optics improves the spatial resolution of Earth-based instruments, Uranus reaped more of the early benefits than its more distant sibling. The priority in observation sessions during the past decade, furthermore, has often been the closer of the two planets, given the interest in observing Uranus pass through the equinox in 2007.

3.7.1 Spatial Variability

Based on *Voyager* data, it is known that Uranus, in 1986, had a slightly varying tropopause temperature, with the lowest temperatures at 25° S, and a second, weaker minimum temperature at 40° N (Flasar et al., 1987). The ortho/para hydrogen ratios were relatively close to equilibrium throughout the planet. Uranian f_p is shown to be within approximately 7% of equilibrium between 0.1 and 1.0 bar, and exhibits some latitudinal north/south asymmetry (Conrath et al., 1998). Beyond this, little spatial variation was detected by *Voyager 2*.

As Uranus approached equinox and telescope technology improved, a different story unfolded, and a richer variety of spatial change was observed. Sromovsky and Fry (2008) develop a 2-cloud model (section 3.5.1) that fits the planet well, though the reflectivity of their deep, 6-8 bar cloud layer increases by about 2% at 33° N, and by about 3-4% in the southern hemisphere. As for the shallow cloud at 2-3 bar, its reflectivity increases about 0.5% at 33° N. The article also notes that at the bright band feature at 43° S, the upper cloud shows a 1% increase in brightness, becomes 25% more reflective, and rises to a higher altitude with 10% less pressure at the cloud top. In addition to the marked changes in the upper cloud at the bright band, the lower cloud moves approximately 1.4 bar deeper. In a similar region, Karkoschka and Tomasko (2009) note that the unusually constant global aerosol opacity in the 1-3 bar region exhibits a spike at 45° S and a gradual decrease north of the equator. Given this almost constant aerosol opacity, they instead explain the brighter high latitudes and darker low latitudes through a change in methane abundance in the 1-3 bar region. Near the equator the methane VMR is 0.032, gradually changing to 0.014 at high southern latitudes.

We have strong evidence on Neptune, however, that stratospheric and tropospheric hazes and weather dynamics are quite varied. These dynamic features range from tens to thousands of kilometres in scale, and remain relatively unstudied. Conrath et al. (1998) found that the ortho/para hydrogen ratio can vary greatly, with f_p diverging by up to about 18% from equilibrium. In the region studied, 20° N to 70° S, the paper also describes a f_p “correlation with latitudinal gradients of the zonal flow.” Some spatial variability in the emission of C₂H₂ has been noted on Neptune, with the lowest emission centred around 50-60° S, and the peaks in emission at the equator and 80° S. The result is interpreted as a result of deep acetylene circulation in which cool acetylene convects upward at mid latitudes, emitting less, and is gradually warmed as it flows away from the midlatitudes, eventually returning to the deep atmosphere at the equator and southern pole (Bézard and Romani, 1991).

3.7.2 Temporal Variability

Uranus’ observational history is one of nearly static, hemispherical asymmetry, an unsurprising result given that the planet’s entire southern hemisphere was in the midst of more than 40 years of daylight, while the north was in perpetual darkness, well before the first *Voyager 2* observations. South polar winds seem to have been fairly constant during this time (Hammel et al., 2005b,a). Sromovsky et al. (2007) model the planet with a 2-layer cloud. The lower cloud, at approximately 4.55 bar, disappears northward of 50° N, and they predict that after the equinox, their model should be reversed with an eventual disappearance of the lower cloud in the south polar region.

Uranus, however, hasn’t been totally devoid of change between the 1986 solstice and the 2007 equinox. Rages et al. (2004) notes HST images that document a bright ring developing at 70° S over 10 years, beginning in 1994. The south pole itself reached a temporal brightness peak in 1994, darkening in the following decade, while the famous polar collar at 45° S brightened in the 2-4 bar pressure level relative to the south pole. Microwave records show a change of more than 30 K in the Uranian disc brightness temperature during the northern winter, and is consistent with changes deep in the atmosphere, at

tens of bars, and unexplainable by solar incidence geometry alone (Klein and Hofstadter, 2006).

Since 2001, this general hemispherical asymmetry and primarily subdued dynamical portrait seen for so much of Uranus' observational history began to evolve rapidly. A large number of major changes have occurred with a similar timescale as those seen prior to 1982, 4 years before the northern winter solstice (Karkoschka, 2001). Winds in Uranus' midlatitudes have accelerated leading into the equinox, and the southern polar collar (45° S) seems to be disappearing while, simultaneously, a new collar at 45° N seems to be appearing as the solar forcing of the planet changes rapidly (Hammel et al., 2005b; Sromovsky et al., 2009; Irwin et al., 2010). Throughout 2006 and 2007, Norwood and Chanover (2009) observe a brightening in the upper, 2-bar cloud layer in the northern hemisphere, while similar clouds in the southern hemisphere dim, just as predicted by Hammel et al. (2006). In 2006 to 2007, Irwin et al. (2010) observes higher cloud reflectance in all latitudes of both cloud layers. In 2007-2008, reduced cloud reflectance in the southern hemisphere and northern mid-latitudes leave comparatively brighter clouds at the equator.

Sromovsky et al. (2003) note that the disc-averaged brightness on Neptune has increased by as much as 40% in just 6 years from in 1996. The disc-averaged result is due to an even more dramatic brightening in certain narrow latitude bands, and is explained by a seasonal model evidencing delayed response to solar incidence due to the planet's obliquity. Observations between 1985 and 2003 show increased ethane emission, followed by a slight decrease in 2004. The observations are consistent with stratospheric temperature changes from 155 to 176 to 165 K, and seem to follow a general seasonal shape, though many unexplained deviations do exist (Hammel et al., 2006; Hammel and Lockwood, 2007).

Orton et al. (2007) describes an interesting hypothesis of a break down in the tropopause cold trap. Observations of an increased tropopause temperature at the southern pole in 2006, just a year after the southern summer solstice, indicate that methane would be able to leak through the cold trap at the pole. The methane leak is facilitated, in theory, by localized polar upwelling of a thermal wave. It is suggested that a similar phenomenon might be observed during every polar summer, helping to feed the active stratospheric

photochemistry on Neptune.

A final interesting point regarding temporal variation on Neptune is the possibility, described in Irwin et al. (2009), that Neptunian haze formation might occur in an episodic manner. Ions or solid particles are necessary to act as nuclei in order for haze particles to condense. Evidence indicates that these particles, most likely derived from the ionization of upper atmosphere molecules by cosmic rays, or meteors descending into the Neptunian atmosphere, are relatively limited in the upper stratosphere. The paper proposes that this lack of condensation nuclei might drive episodic periods of hydrocarbon supersaturation followed by rapid haze formation.

Chapter 4

Results

The initial data developed throughout the graduate studies described here have been obtained from NASA's Infrared Telescope Facility (IRTF) using an infrared spectrometer known as SpeX. This chapter provides an overview of the telescope and spectrometer, the associated dataset, some of the unique processing requirements that must be addressed prior to running NEMESIS retrievals, and a few preliminary retrieval results.

4.1 IRTF Observations

NASA's IRTF is a 3.0 meter telescope operated by the University of Hawaii's Institute for Astronomy. The IRTF is located near the summit of Mauna Kea, Hawaii, where the high altitude (4200 m) and relatively dry, stable climate create a very low airmass above the telescope. This helps minimize telluric features in the telescope's observations. SpeX is a medium resolution spectrograph with a spectral range of 0.8-5.4 μm , and was purpose-built by the Institute for Astronomy.

The data for this work is derived from the short wavelength, cross-dispersed mode (SXD) that operates between 0.8 and 2.4 μm . Raw data from the SXD viewing mode is sorted into six 'orders' using cross-dispersing prisms (Rayner et al., 2003). Within each order, the central line is where the strongest signal is received, while signal strength decays to

Table 4.1: Wavelength Specifications for SpeX SXD Mode

<i>Order</i>	<i>Wavelengths (microns)</i>	<i>Window Name</i>
8	0.81 - 0.90	I
7	0.81 - 1.03	z
6	0.94 - 1.20	J1
5	1.13 - 1.45	J2
4	1.41 - 1.81	H
3	1.88 - 2.42	K

either side. The effective viewing ranges of each of the six orders (identified with order numbers 3 through 8) are summarized in table 4.1.

Table 4.2 details the relevant elements of the IRTF dataset captured on three nights in August, 2009. These data were acquired using the SpeX SXD mode with a 0.5×15.0 arcsecond slit. Given this slit size, the data has a spectral resolution of about $R = 1,200$. The data is imaged at $0.15'' \cdot \text{pixel}^{-1}$ onto a 1024×1024 pixel array providing a slit length of 100 pixels. (Rayner et al., 2003). Resolving power has been calculated by determining the number of pixels at full-width-half-maximum for each stellar observation, and multiplying by the $0.15'' \cdot \text{pixel}^{-1}$ array value.

4.2 Image Processing

4.2.1 SpeXtool

An IDL software package, SpeXtool, assists with the image processing. The software takes raw data and produces all the necessary calibration files, including flat-fielding files used to normalize all observations to the same ‘0’ levels. SpeXtool works quite well for point sources, like our solar standard observations, and operates by automatically finding the strongest signal and producing a spectral output for the observed star in each order of the SXD mode. Figure 4.1 shows the data for a standard star observation that is input into SpeXtool. The upper frames of figures 4.5 and 4.6 contain plots of the final SpeXtool output of solar standards.

Table 4.2: Observation Log

<i>Date</i>	<i>Target</i>	<i>Time (UT)</i>	<i>Duration (seconds)</i>	<i>Resolving Power (arc seconds)</i>	<i>Air Mass</i>
18Aug09	HD1160 (G2 Standard)	14:36	30	0.525± 0.075	1.156
		14:37	30		1.159
	Uranus	14:50	60	0.525± 0.075	1.370
		14:52	120		1.382
		14:57	120		1.409
		15:04	120		1.447
		15:07	120		1.460
		15:12	120		1.490
		15:16	120		1.521
	SAO146912 (A0 Standard)	15:24	60	0.525± 0.075	1.561
15:27		60		1.583	
25Aug09	HD1160 (G2 Standard)	14:53	30	0.525± 0.075	1.305
		14:55	30		1.321
	Uranus	15:04	120	0.525± 0.075	1.657
		15:06	120		1.660
		15:11	120		1.700
		15:25	120		1.850
	SAO146912 (A0 Standard)	15:37	60	1.050± 0.075	1.950
28Aug09	HD1160 (G2 Standard)	10:50	30	0.600± 0.075	1.100
		10:52	30		1.100
		10:54	30		1.094
	Uranus	11:05	120	0.600± 0.075	1.093
		11:10	120		1.090
		11:30	120		1.092
		–	120		–
	SAO146912 (A0 Standard)	11:58	60	0.750± 0.075	1.085
	Neptune	12:33	120		1.678
	SAO146912 (A0 Standard)	13:18	60	0.750± 0.075	1.186
	Uranus	13:53	120	0.750± 0.075	1.304
		–	120		–
		14:13	120		1.394
		–	120		–
	HD1160 (G2 Standard)	15:00	30	0.825± 0.075	1.395
		15:02	30		1.401
	Uranus	15:13	120	0.825± 0.075	1.842
		15:15	120		1.873
	SAO146912 (A0 Standard)	–	120	1.275 ± 0.075	–
		15:24	120		1.981



Figure 4.1: Sample of IRTF standard star observation prior to processing in SpeXtool. The first frames in figures 4.5 and 4.6 show plots of the SpeXtool output for standard star observations.

Unfortunately, SpeXtool does not handle extended sources as thoroughly. SpeXtool is capable of combining back-to-back observations to produce average observations when an object has been viewed several times in a row with the spectrometer. After combining observations and producing flat-fielded, calibrated images, however, it does not correct the curves in the raw images. Figure 4.2 shows a SpeXtool input and output for sample Uranus observation.

For extended sources, the remaining processing cannot be done in SpeXtool. Major tasks include:

- Combining orders of solar standards into continuous spectra
- Determining where in each data cube the central point of extended source (planet) observations occurs for each order
- Extracting a radiance plot for each order and for each planet observation
- Dividing out stellar standards from each observation to remove any telluric absorption features

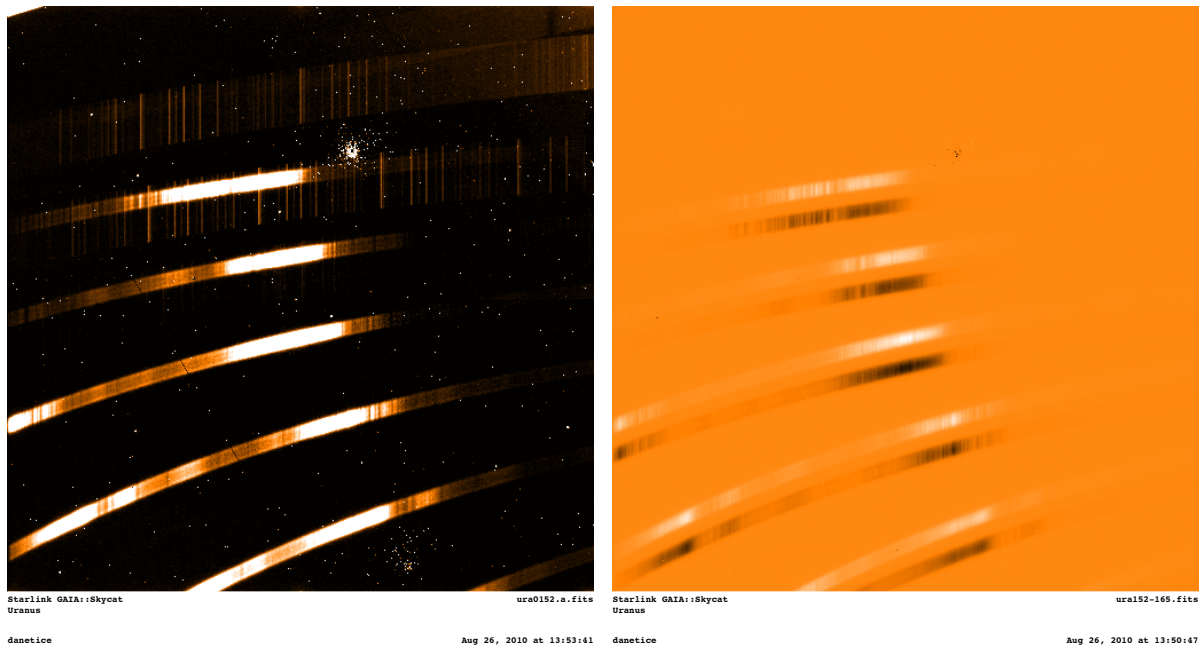


Figure 4.2: Sample of IRTF Uranus observation. Left frame is raw data from SpeX, right frame is final processed form output from SpeXtool.

- Correcting for any differences in airmass between observations and standards
- Determining a reliable photometric value to convert output units from counts to radiance

Though the first four of these steps have been completed, improvements to the handling of solar standards and a more complete analysis of the differences between the A0 and G2 stellar standards will be necessary.

4.2.2 Further Data Processing

Completion of data processing on SpeXtool outputs requires a final processing code that corrects for the curves in the observations and divides the results by the solar standards. This code is in development and will produce an observation which, in theory, corrects for telluric absorption interference, and from which it is possible to plot values in a straightforward manner. Figure 4.3 shows an example of an observation of Uranus after undergoing the final processing routine, and 4.4 shows a plot of the resulting spectrum.



Figure 4.3: Sample of calibrated, flat-fielded, and telluric corrected SpeX data file after extended processing routine.

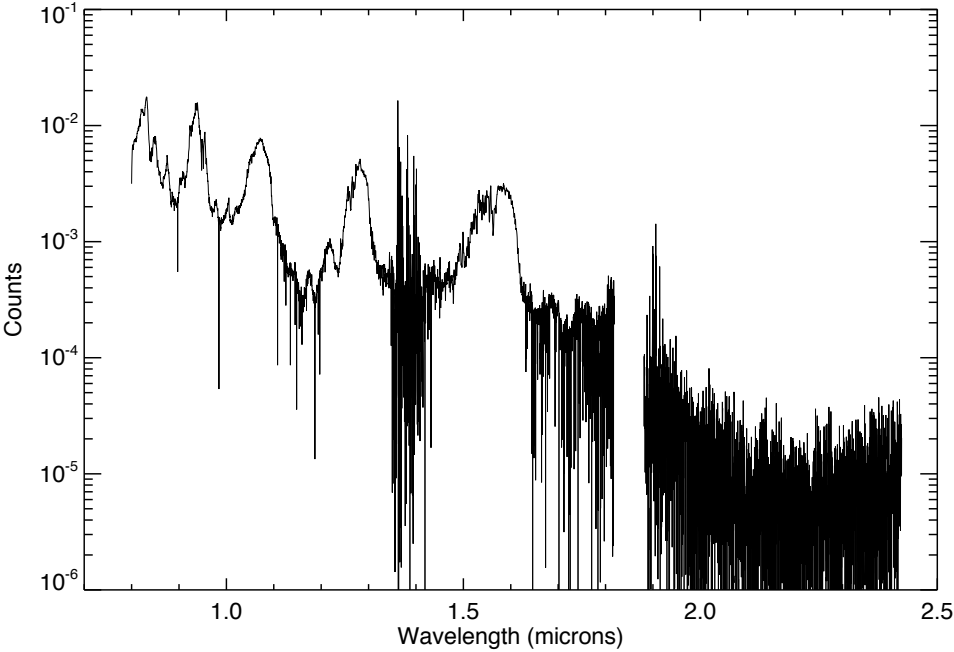


Figure 4.4: Sample plot of disc-averaged, IRTF observation spectrum.

4.2.3 Solar Standards

Sample plots of both stellar standard types, along with a plot of their current, normalised forms appear in figures 4.5 and 4.6. Each order was fitted with a quadratic-gaussian best-fit curve based on the region of high signal-to-noise within each order, in order to map the spectra of the six SXD orders onto the continuous, normalised spectrum shown. Once completed, overlapping regions in each order were averaged to produce final, continuous ‘count’ profiles. Once a reliable photometric value is established, this profile will simply be multiplied by the appropriate value to convert it into a radiance spectrum. Until a reliable photometric is determined, the original six spectra are divided by the Planck function for the star’s temperature prior to the best-fit and averaging routines, and multiplied by the same Planck function at the end of the process.

4.3 Preliminary Retrievals

Figure 4.7 shows a sample of a retrieved spectrum from NEMESIS plotted over a sample set of Gemini data for a 45° emission angle. For comparative purposes, the sample data is limited to the same, more limited spectral range as UKIRT data. Figure 4.8 shows the aerosol opacity retrieved by NEMESIS, and based upon the Gemini sample data. The results agree with UKIRT analysis which identifies a prominent cloud deck at 2-3 mbar (Irwin et al., 2007, 2009, 2010), and confirm that the retrieval procedure is working as intended.

Figures 4.9 and 4.10 show corresponding results from a sample IRTF dataset, again limited to the same spectral range as UKIRT data. The data has been disc-averaged and artificially scaled in order to make a comparison with the 45° emission angle Gemini results because IRTF processing routines are not yet complete. From figure 4.9 it is clear that the observed spectrum is not fit well by the forward model. We attribute this to the noise that appears in the data between 1.6 and 1.8 μm . This region is characterised by strong CH_4 absorption which should effectively eliminate observed radiance, as seen

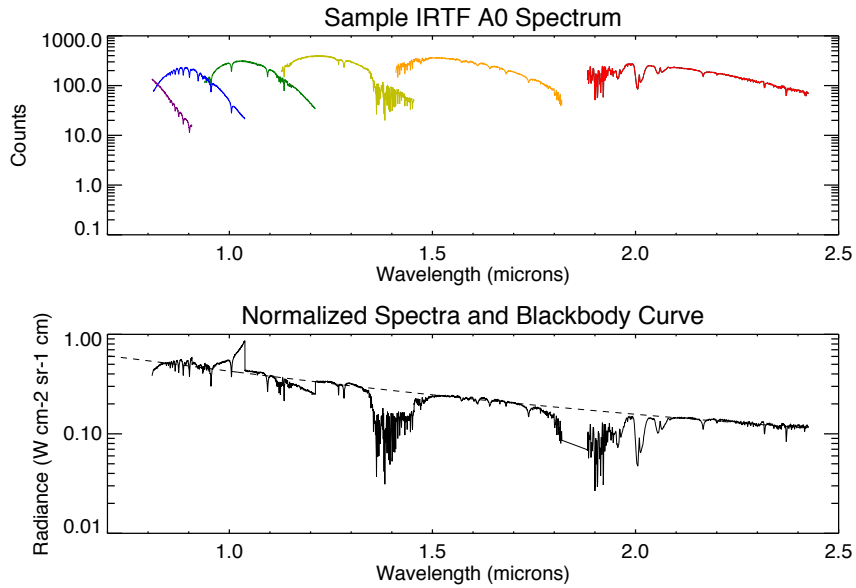


Figure 4.5: Sample A0 Standard Star. SpeXtool processed form (upper frame) and normalized form (lower frame). Observation data (solid lines) and 10,800 K Planck function for comparison (dashed line). Various colours in upper plot differentiate between SXD orders 3-8 (see figure 4.1).

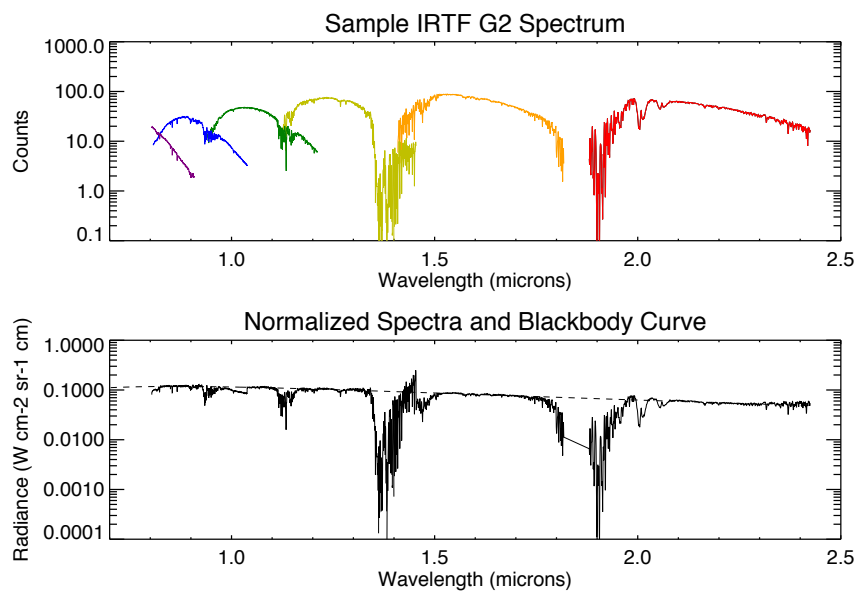


Figure 4.6: Same as figure 4.5 but for G2 Standard Star and 5,920 K Planck function

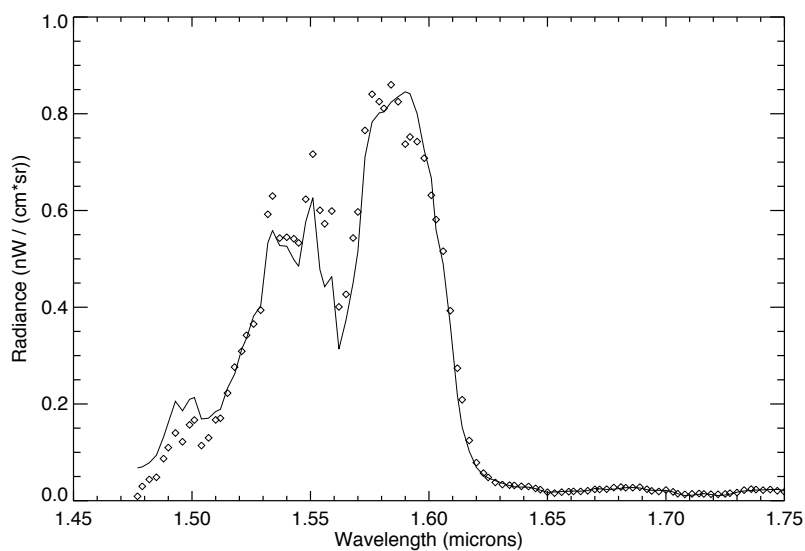


Figure 4.7: Gemini-observed (diamonds) and NEMESIS-retrieved (line) spectrum.

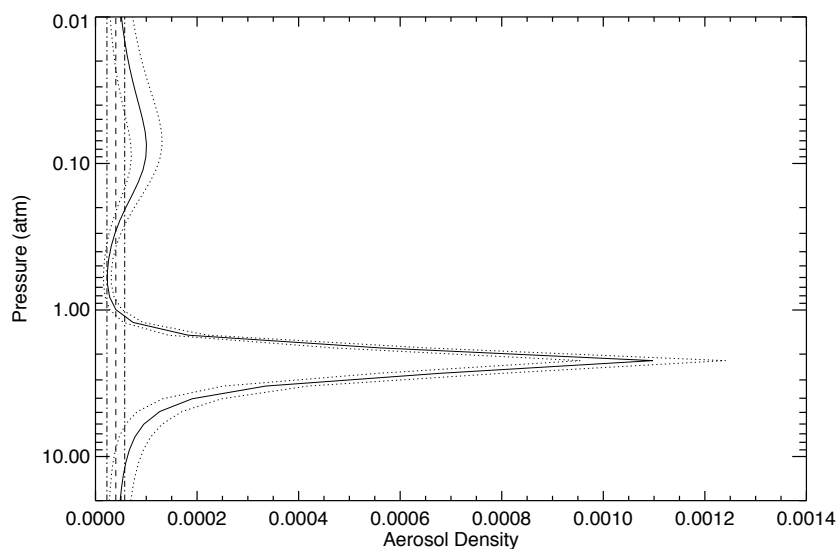


Figure 4.8: Sample of Uranus aerosol opacity profile. Retrieval (solid) and associated error (dotted); *a priori* (dashed) and associated error (dash-dotted).

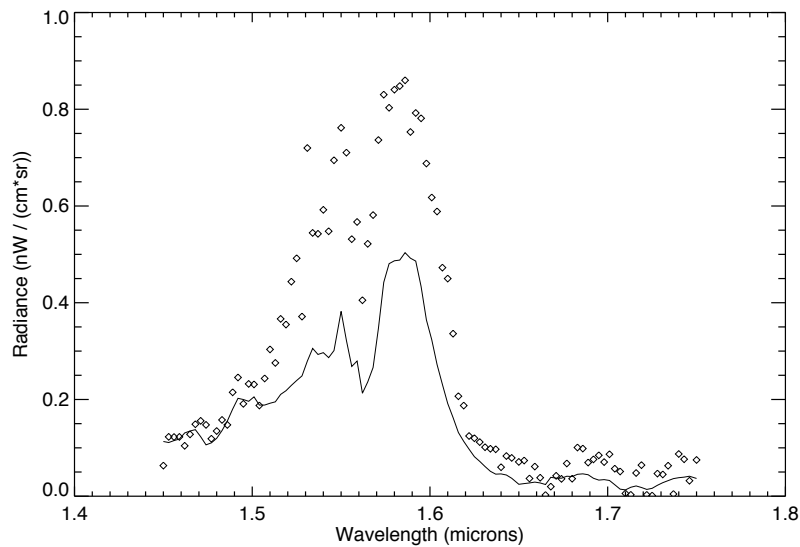


Figure 4.9: Same as figure 4.7 but for disc-averaged IRTF data.

in the Gemini data in figure 4.7. The noise indicates that there are calibration problems which must be addressed before retrievals can be considered reliable.

The retrieval code interprets this spurious ‘radiance’ as scattering from stratospheric haze, and consequently produces a model with a stratospheric haze much thicker than reality. The result of this thick haze layer is that not enough light is able to pass through to the troposphere to observe the 2-3 bar cloud deck. Regardless of single scattering albedos of this haze, which were adjusted in an effort to pass more light through the atmosphere to the 2-3 bar level, the model is unable to see the cloud deck. Figure 4.10 shows the IRTF retrieval which most closely matched the Gemini / UKIRT results. This result was obtained using a single scattering albedo of 1.0, and is still unable to resolve the deep cloud layer.

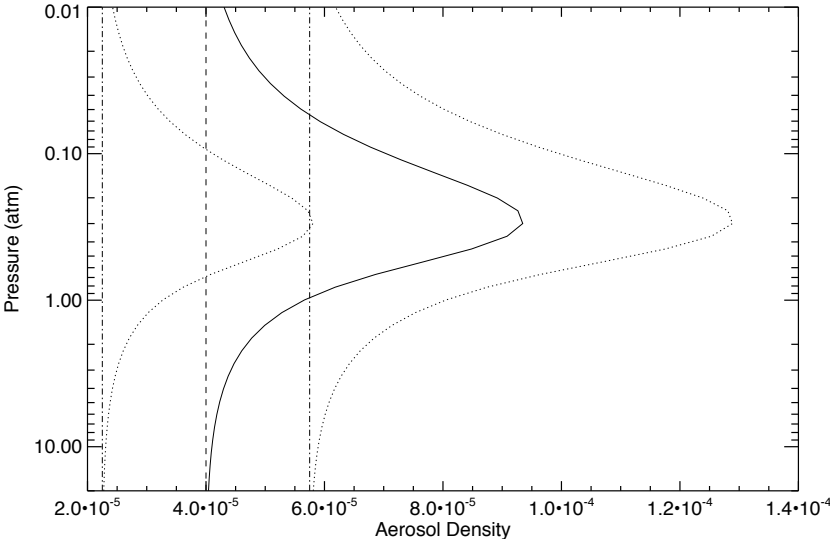


Figure 4.10: Same as figure 4.8 but for disc-averaged IRTF observation.

Chapter 5

Future Work

5.1 Data Processing

Before analysis of the data can begin in earnest, several final steps of data processing must be undertaken, as described below.

5.1.1 Stellar Standard Analysis

Before a complete analysis can be undertaken of the stellar standards produced by SpeX-tool, the method of normalizing the radiances across each of the six orders must be improved. Currently, there are some clear regions where the normalising routine is not working well and this problem must be addressed. Additionally, the averaging of order overlap must be modified, incorporating weighted averages based on uncertainty values rather than the current, unweighted averaging scheme.

Once modifications are made, a comparison with a Planck curve for an idealized black body at the star's temperature can be performed. Differences between the standard observation and black body curve will help identify what absorption features are evident in the standard observations. Comparison between the two types of stars included in standard observations (A0 and G2) will help identify which features are unique to the star, and which come from absorption lines within Earth's atmosphere.

After this analysis, questions that must be addressed include determining which standard star type is the best suited to use when correcting ice giant observations for stellar and telluric absorption features, and what impact, if any, stellar and telluric absorption features will have on retrievals in the near-IR.

NEMESIS uses a solar standard profile to generate the solar spectrum which is incident on the retrieval objects. It has been discovered that this standard is a rather old one, taken from Houghton 2002, and contains a very coarse grid scale. Before any earnest data analysis is possible, it must be ensured that the scale on this standard is sufficient to include all features that are evident in the stellar standard observations. It seems likely that NEMESIS' solar standard file will prove too coarse, which will require a new, more finely-gridded standard file to be found and incorporated.

5.1.2 Air Mass

The mass of the air column through which the telescope views has an important impact on the results of the observations, despite the thinness of the atmosphere at 2400 metres. Because the Earth's atmosphere contains absorbers, most notably H_2O , even the smallest column abundance of these absorbers will add features to the observation which are not elements of the planet's spectrum, but are telluric in origin.

Before retrieval results may be considered valid, it must be determined whether air mass differences between standard observations and planet observations will adversely impact the telluric correction routines. In most cases the air mass difference is quite minimal as the time between viewing the standard and the planet is on the order of minutes. There are some cases, however, where the air mass difference might be nontrivial as the closest standard is separated from the planet observation by a time difference on the order of hours. While atmospheric conditions on Mauna Kea are quite well suited to telescopic data collection, diagnostics must still be run to ensure that the corrections are indeed removing an appropriate amount of telluric features.

5.2 Choosing a Focused Thesis Topic

Once the last data processing needs are satisfied, the next major goal is to run retrievals on the data to assess what sort of information can be gleaned. The first trustworthy retrievals will help to refine the specific topic and research goals for future graduate work, so that a specific thesis may be developed. Several possible research areas, outlined below, are both accessible given the dataset, and in need of further study.

5.2.1 IRTF Data

One of the strengths of the IRTF data is its wide spectral range. Spanning 0.8-2.4 μm , the data will allow extended analysis of two of the most important ice giant atmospheric constituents, clouds and methane, far beyond properties that were accessible to recent UKIRT analysis at Oxford (Irwin et al., 2007, 2009, 2010). Given the wide spectral window available, as well as the good spatial resolution, it will be possible to determine much tighter constraints on cloud particle size and distribution than available with UKIRT, as well as studying how these properties vary with latitude.

A very important tool available with IRTF data is a reliable way of distinguishing between NH_3 abundance and cloud opacity. Studies based on narrow IR spectral regions have no way to identify the smaller effects due to aerosol opacity because NH_3 absorption features in most spectral regions dominate the reflectivity of the atmospheres. As described in Karkoschka and Tomasko (2009), the usual solution is to assume that the NH_3 mixing ratio is independent of latitude and time. This solution, probably reasonable for the gas giants, allows any variation in reflectivity to be attributed exclusively to changes in aerosol opacity. On the ice giants, however, the NH_3 mixing ratio varies by three orders of magnitude in the upper troposphere alone, implying that its abundance might behave like that of terrestrial water vapor, which varies dramatically with both time and latitude. Given IRTF's data in the 0.820-0.834 μm region, we can avoid this unrealistic assumption. In this spectral band, collision-induced absorption by H_2 molecules dominates NH_3 absorption. If opacity variations are evident outside this narrow spectral band but not

inside, it can be verified that the change is due to changes in NH_3 abundance. If variation in opacity is observed both inside and outside this narrow spectral region, it can be attributed to aerosol opacity.

Currently, no spectral identifiers have been determined for the deep cloud deck, and it is therefore assumed to be H_2S or NH_3 , as this result would be consistent with the ECCM. With a more reliable way of determining NH_3 abundance as well as a more complete characterisation of cloud particle size and distributions, we have much more information to apply to the question of cloud deck composition, and may be able to positively identify its molecular composition.

5.2.2 Other Available Data

It will also be possible to build upon results from other ice giant observations. IRTF data might be used to extend and elaborate upon published results from the United Kingdom Infra-Red Telescope (UKIRT) and current and future analysis of observations from Gemini-North.¹ The planetary physics group at the University of Oxford has acquired ice giant data from UKIRT, IRTF, and Gemini over a time span of 2006 to 2009. More observation time on Gemini-North is secured in 2010. With a 5-year timespan of observations, a unique opportunity to look at temporal variation on Uranus and Neptune has been created. With Uranus moving through its equinox in the middle of this observational series, its atmospheric changes during the data series are of particular interest.

In addition to unique opportunities to characterise temporal change, Gemini data, in particular, contains a very high degree of spatial resolution, capable of resolving small-scale features like storms and convection clouds. This data might provide a nice complement to study of the IRTF data, allowing further characterisation of discrete features on the ice giants.

¹UKIRT has an imager-spectrometer (UIST) that operates between 1 and 5 μm , while Gemini north has a near-IR spectrometer (NIFS) that images between 0.95 and 2.40 μm and a near-IR imager and spectrometer (NIRI) that operates between 1 and 5 μm .

5.2.3 Improved Methane Absorption Data

Nearly all of the analysis described in the literature review (the notable exception being Irwin et al. (2010)) included in this report were performed prior to the latest set of methane absorption data presented in Karkoschka and Tomasko (2010). These new coefficients, which can be applied to any of the above areas of study, are shown to be more accurate at the lower temperatures associated with the observable ice giant atmospheres. Coefficients used in previous analyses have been as many as two orders of magnitude separated from these new values. The impact of this on any retrieval conclusions based on spectra from the 0.4-5.5 μm region could be substantial. Therefore, even if the thesis focus overlaps with previous work, the more accurate methane absorption data will provide increased accuracy when compared to older studies.

5.3 Graduate Study Timeline

Once a focused thesis topic is determined, more time will be spent analysing the data and working to combine it with any applicable UKIRT or Gemini data. A projected timeline for the next 24 months of study is included in table 5.1.

Table 5.1: Projected Timeline

<i>Projected Completion</i>	<i>Time Allowed (months)</i>	<i>Task</i>
Sep 2010	1	Full Analysis and Comparison of A0 and G2 Stellar Standards Analyse and Correct Observations for Changes in Airmass Determine Correct Photometric Conversion Values
Oct 2010	1	Run Basic Retrievals for all Observations
Nov 2010	1	Selection of Specific Thesis Research Goals;
Feb 2011	3	Further Retrievals and Tuning
Mar 2011	1	Determine what UKIRT / Gemini Results Will Strengthen Thesis
June 2011	3	Data Processing (if necessary) and Retrievals of UKIRT & Gemini Data
August 2011	2	Write Second Year Report
May 2012	9	Combing Applicable Results with UKIRT/Gemini Results Further Retrievals and Analysis
August 2012	3	Write Thesis

Bibliography

Andrews, D. G. (2000). *An Introduction to Atmospheric Physics*. Cambridge University Press, Cambridge UK.

Atreya, S., Egeler, P., and Baines, K. (2006). Water-ammonia ionic ocean on Uranus and Neptune? *Geophys. Res. Abs.*, 8.

Baines, K. H. and Bergstralh, J. T. (1986). The structure of the Uranian atmosphere: Constraints from the geometric albedo spectrum and H₂ and CH₄ line profiles. *Icarus*, 65:406–441.

Baines, K. H. and Hammel, H. (1994). Clouds, hazes, and stratospheric methane abundance in Neptune. *Icarus*, 109:20–39.

Baines, K. H., Hammel, H. B., Rages, K. A., Romani, P. N., and Samuelson, R. E. (1995a). *Neptune and Triton*, chapter Clouds and hazes in the atmosphere of Neptune, pages 489–546. University of Arizona Press, Tucson.

Baines, K. H., Mickelson, M. E., Larson, L. E., and Ferguson, D. W. (1995b). The abundances of methane and ortho-para hydrogen on Uranus and Neptune: Implications of new laboratory 4-0 H₂ quadrupole line parameters. *Icarus*, 144:328–340.

Bishop, J., Atreya, S. K., Romani, P. N., Orton, G. S., Sandel, B. R., and Yelle, R. V. (1995). *Neptune and Triton*, chapter The Middle and Upper Atmosphere of Neptune, pages 427–488. University of Arizona Press, Tucson.

Burgdorf, M., Orton, G. S., Davis, G. R., Sidher, S. D., Feuchtgruber, H., Griffin, M. J., and Swinyard, B. M. (2003). Neptune’s far-infrared spectrum from the ISO long-wavelength and short-wavelength spectrometers. *Icarus*, 164:244–253.

- Burgdorf, M., Orton, G. S., van Cleve, J., Meadows, V., and Houck, J. (2006). Detection of new hydrocarbons in Uranus' atmosphere by infrared spectroscopy. *Icarus*, 184:634–637.
- Bézard, B., Drossart, P., Encrenaz, T., and Feuchtgruber, H. (2001). Benzene on the Giant Planets. *Icarus*, 154:492–500.
- Bézard, B. and Romani, P. (1991). Hydrocarbons in Neptune's stratosphere from Voyager infrared observations. *J. Geophys. Res. Planets*, 96:18961–18975.
- Bézard, B., Romani, P. N., Feuchtgruber, H., and Encrenaz, T. (1999). Detection of the methyl radical on Neptune. *Astrophys. J.*, 515:868–872.
- Cavalié, T., Billebaud, F., Fouchet, T., Lellouch, E., Brillet, J., and Dobrijevic, M. (2008). Observations of CO on Saturn and Uranus at millimetre wavelengths: new upper limit determinations. *Astron. Astrophys.*, 484:551–561.
- Conrath, B., Flasar, F. M., Hanel, R., Kunde, V., Maguire, W., Pearl, J., Pirraglia, J., Sameulson, R., Gierasch, P., Weir, A., Bézard, B., Gautier, D., Curuikshank, D., Horn, L., Springer, R., and Shaffer, W. (1989). Infrared observations of the Neptunian System. *Science*, 246:1454–1459.
- Conrath, B. J., Gautier, D., Hanel, R., Lindal, G., and Marten, A. (1987). The helium abundance of Uranus from Voyager measurements. *J. Geophys. Res. Space Phys.*, 92:15003–15010.
- Conrath, B. J., Gautier, D., Lindal, G. F., Samuelson, R. E., and Shaffer, W. A. (1991a). The helium abundance of Neptune from Voyager measurements. *J. Geophys. Res. Planets*, 96:18907–18919.
- Conrath, B. J., Gautier, D., Owen, T. C., and Samuelson, R. E. (1993). Constraints on N₂ in neptune's atmosphere from Voyager measurements. *Icarus*, 101:168–172.
- Conrath, B. J., Gierasch, P. J., and Ustinov, E. A. (1998). Thermal structure and para hydrogen fraction on the outer planets from Voyager IRIS measurements. *Icarus*, 135:501–517.

- Conrath, B. J., Pearl, J. C., Appleby, J. F., Linal, G. F., Orton, G. S., and Bézard, B. (1991b). *Uranus*, chapter Thermal structure and energy balance of Uranus, pages 204–252. University of Arizona Press, Tucson.
- Courtin, R., Gautier, D., and Stobel, D. (1996). The CO abundance on Neptune from HST observations. *Icarus*, 123:37–55.
- Cushing, M. C., Vacca, W. D., and Rayner, J. T. (2004). Spextool: A spectral extraction package for SpeX, a 0.8-5.5 micron cross-dispersed spectrograph. *Publ. Astron. Soc. Pac.*, 116:362–376.
- de Bergh, C., Lutz, B. L., Owen, T., Brault, J., and Chauville, J. (1986). Monodeuterated methane in the outer solar system. II: Its detection on Uranus at 1.6 microns. *Astrophys. J.*, 311:501–510.
- de Bergh, C., Lutz, B. L., Owen, T., and Maillard, J. P. (1990). Monodeuterated methane in the outer solar system: IV: Its detection and abundance on Neptune. *Astrophys. J.*, 355:661–666.
- de Pater, I., Gibbard, S. G., Macintosh, B. A., Roe, H. G., Gavel, D. T., and Max, C. E. (2002). Keck adaptive optics images of Uranus and its rings. *Icarus*, 160:359–374.
- de Pater, I. and Massie, S. (1985). Models of millimetre-centimetre spectra of the giant planets. *Icarus*, 62:143–171.
- de Pater, I., Romani, P. N., and Atreya, S. K. (1991). Possible microwave absorption by H₂S gas in Uranus’ and Neptune’s atmospheres. *Icarus*, 91:220–233.
- Dudhia, A., Jay, V. L., and Rodgers, C. D. (2002). Microwindow selection for high-spectral-resolution sounders. *Appl. Optics*, LP 41:3665–3673.
- Encrenaz, T. (2004). Neutral atmospheres of the giant planets: an overview of composition measurements. *Space Sci. Rev.*, 116:99–119.
- Encrenaz, T., Feuchtgruber, H., Atreya, S. K., Bézard, B., Lellouch, E., Bishop, J., Edgington, S., de Graauw, T., Griffin, M., and Kessler, M. F. (1998). ISO observations

- of Uranus: The stratospheric distribution of C_2H_2 and the eddy diffusion coefficients. *Astron. Astrophys.*, 333:L42–L46.
- Encrenaz, T., Lellouch, E., Drossart, P., Feuchtgruber, H., Orton, G. S., and Atreya, S. K. (2004). First detection of CO in Uranus. *Astron. Astrophys.*, 413:L5–L9.
- Encrenaz, T., Serabyn, E., and Weisstein, E. W. (1996). Millimeter spectroscopy of Uranus and Neptune: Constraints on CO and PH_3 tropospheric abundances. *Icarus*, 124:616–624.
- Feuchtgruber, H., Lellouch, E., Bézard, B., Encrenaz, T., de Graauw, T., and Davis, G. R. (1999). Detection of HD in the atmospheres of Uranus and Neptune: a new determination of the D/H ratio. *Astron. Astrophys.*, 341:L17–L21.
- Feuchtgruber, H., Lellouch, E., de Graauw, T., Bézard, B., Encrenaz, T., and Griffin, M. (1997). External supply of oxygen to the atmospheres of the Giant Planets. *Nature*, 389:159.
- Flasar, F. M., Conrath, B. J., Gierasch, P. J., and Pirraglia, J. A. (1987). Voyager infrared observations of Uranus' atmosphere: Thermal structure and dynamics. *J. Geophys. Res. Space Phys.*, 92:15011–15018.
- Fletcher, L. N., Drossart, P., Burgdorf, M., Orton, G. S., and Encrenaz, T. (2010). Neptune's atmospheric composition from AKARI infrared spectroscopy. *Astron. Astrophys.*, 514:A17.
- Fouchet, T., Lellouch, E., and Feuchtgruber, H. (2003). The hydrogen ortho-to-para ratio in the stratospheres of the giant planets. *Icarus*, 161:127–143.
- Gibbard, S. G., de Pater, I., Roe, H. G., Martin, S., Macintosh, B. A., and Max, C. E. (2003). The altitude of Neptune cloud features from high-spatial-resolution near-infrared spectra. *Icarus*, 166:359–374.
- Gibbard, S. G., Roe, H., de Pater, I., Macintosh, B., Gavel, D., Max, C. E., Baines, K. H., and Ghez, A. (2002). High-resolution infrared imaging of Neptune from the Keck Telescope. *Icarus*, 156:1–15.

- Goody, R. M. and Yung, Y. L. (1989). *Atmospheric Radiation: Theoretical Basis*. Oxford University Press, 2nd edition.
- Guilloteau, S., Dutrey, A., Marten, A., and Gautier, D. (1993). Co in the troposphere of Neptune: Detection of the $J = 1 - 0$ line in absorption. *Astron. Astrophys.*, 279:661–667.
- Hammel, H. B., de Pater, I., Gibbard, S., Lockwood, G. W., and Rages, K. (2005a). New cloud activity on Uranus in 2004: First detection of a southern feature at $2.2 \mu\text{m}$. *Icarus*, 175:284–288.
- Hammel, H. B., de Pater, I., Gibbard, S., Lockwood, G. W., and Rages, K. (2005b). Uranus in 2003: Zonal winds, banded structure, and discrete features. *Icarus*, 175:534–545.
- Hammel, H. B. and Lockwood, G. W. (2007). Long-term atmospheric variability on Uranus and Neptune. *Icarus*, 186:291–301.
- Hammel, H. B., Lynch, D. K., Russel, R. W., Sitko, M. L., Bernstein, L. S., and Hewagama, T. (2006). Mid-infrared ethane emission on Neptune and Uranus. *Astrophys. J.*, 644:1326–1333.
- Hammel, H. B., Rages, K., Lockwood, G. W., Karkoschka, E., and de Pater, I. (2001). New measurements of the winds of Uranus. *Icarus*, 153:229–235.
- Hammel, H. B., Sitko, M. L., Lynch, D. K., Orton, G. S., Russel, R. W., Geballe, T. R., and de Pater, I. (2007). Distribution of ethane and methane emission on Neptune. *Astron. J.*, 134:637–641.
- Hammel, H. B., Sromovsky, L. A., Fry, P. M., Rages, K., Showalter, M., de Pater, I., van Dam, M. A., LeBeau, R. P., and Deng, X. (2009). The Dark Spot in the atmosphere of Uranus in 2006: Discovery, description, and dynamical simulations. *Icarus*, 201:257–271.
- Herbert, F. and Sandel, B. R. (1999). Ultraviolet observations of Uranus and Neptune. *Planet. Space Sci.*, 47:1119–1139.
- Hesman, B. E., Davis, G. R., Matthews, H. E., and Orton, G. S. (2007). The abundance profile of CO in Neptune’s atmosphere. *Icarus*, 186:342–353.

- Horne, K. (1986). An optimal extraction algorithm for CCD spectroscopy. *Publ. Astron. Soc. Pac.*, 98:609–617.
- Houghton, J. (2002). *The Physics of Atmospheres*. Cambridge University Press, 3rd edition.
- Irwin, P. G. J. (2009). *Giant Planets of our Solar System: Atmospheres, Composition, and Structure*. Praxis Publishing Ltd, Chichester, UK, 2nd edition.
- Irwin, P. G. J., Teanby, N. A., and Davis, G. R. (2007). Latitudinal variations in Uranus' vertical cloud structure from UKIRT UIST observations. *Astrophys. J.*, 665:L71–L74.
- Irwin, P. G. J., Teanby, N. A., and Davis, G. R. (2009). Vertical cloud structure of Uranus from UKIRT/UIST observations and changes seen during Uranus' northern spring equinox from 2006 to 2008. *Icarus*, 203:287–302.
- Irwin, P. G. J., Teanby, N. A., and Davis, G. R. (2010). Revised vertical cloud structure of Uranus from UKIRT/UIST observations and changes seen during Uranus' Northern Spring Equinox from 2006 to 2008: Application of new methane absorption data and comparison with Neptune. *Icarus*, 208:913–926.
- Irwin, P. G. J., Teanby, N. A., de Kok, R., Fletcher, L. N., Howett, C. J. A., Tsang, C. C. C., Wilson, C. F., Calcutt, S. B., Nixon, C. A., and Parrish, P. D. (2008). The NEMESIS planetary atmosphere radiative transfer and retrieval tool. *J. Quant. Spectrosc. Ra.*, 109:1136–1150.
- Karkoschka, E. (1998). Clouds of high contrast on Uranus. *Science*, 280:570.
- Karkoschka, E. (2001). Uranus' apparent seasonal variability in 25 HST filters. *Icarus*, 151:84–92.
- Karkoschka, E. and Tomasko, M. (2009). The haze and methane distributions on Uranus from HST-STIS spectroscopy. *Icarus*, 202:287–309.
- Karkoschka, E. and Tomasko, M. (2010). Methane absorption coefficients for the Jovian planets from laboratory, Huygens, and HST data. *Icarus*, 205:674–694.

- Klein, M. J. and Hofstadter, M. D. (2006). Long-term variations in the microwave brightness temperature of the Uranus atmosphere. *Icarus*, 184:170–180.
- Lacis, A. A. and Oinas, V. (1991). A description of the correlated kappa-distribution method for modeling nongray gaseous absorption, thermal emission, and multiple-scattering in vertically inhomogeneous atmospheres. *J. Geophys. Res. Atmos.*, 96:9027–9063.
- Lellouch, E., Romani, P., and Rosenqvist, J. (1994). The vertical distribution and origin of HCN in Neptune’s atmosphere. *Icarus*, 108:112–136.
- Lian, Y. and Showman, A. P. (2010). Generation of equatorial jets by large-scale latent heating on the giant planets. *Icarus*, 207:373–393.
- Lindal, G. F. (1992). The atmosphere of Neptune: an analysis of radio occultation data acquired with Voyager 2. *Astron. J.*, 103:967–982.
- Lindal, G. F., Lyons, J. R., Sweetnam, D. N., Eshleman, V. R., Hinson, D. P., and Tyler, G. L. (1987). The atmosphere of Uranus: Results of radio occultation measurements with Voyager 2. *J. Geophys. Res. Space Phys.*, 92:14987–15001.
- Lodders, K. and Fegley, Jr., B. (1994). The origin of carbon monoxide in Neptune’s atmosphere. *Icarus*, 112:368–375.
- Marley, M. S. and McKay, C. P. (1999). Thermal structure of Uranus’ atmosphere. *Icarus*, 138:268–286.
- Marten, A., Gautier, D., Owen, T., Sanders, D. B., Matthews, H. E., Atreya, S. K., Tilanus, R. P. J., and Deane, J. R. (1993). First observations of CO and HCN on Neptune and Uranus at millimetre wavelengths and their implications for atmospheric chemistry. *Astrophys. J.*, 406:285–297.
- Marten, A., Matthews, H. E., Owen, T., Moreno, R., Hidayat, T., and Biraud, Y. (2005). Improved constraints on Neptune’s atmosphere from submillimetre-wavelength observations. *Astron. Astrophys.*, 429:1097–1105.

- Massie, S. T. and Hunten, D. M. (1982). Conversion of para- and ortho-hydrogen in the Jovian planets. *Icarus*, 143:244–298.
- Max, C. E., Macintosh, B. A., Gibbard, S. G., Gavel, D. T., Roe, H. G., de Pater, I., Ghez, A. M., Acton, D. S., Lai, O., Stomski, P., and Wizinowich, P. L. (2003). Cloud structures on Neptune observed with Keck Telescope adaptive optics. *Astron. J.*, 125:364–375.
- Meadows, V. S., Orton, G., Line, M., Liang, M., Yung, Y. L., Cleve, J. V., and Burgdorf, M. J. (2008). First Spitzer observations of Neptune: Detection of new hydrocarbons. *Icarus*, 197:585–589.
- Naylor, D. A., Davis, G. R., Griffin, M. J., Clark, T. A., Gautier, D., and Marten, A. (1994). Broad-band spectroscopic detection of the CO J = 3 - 2 tropospheric absorption in the atmosphere of Neptune. *Astron. Astrophys.*, 291:L51–L53.
- Norwood, J. W. and Chanover, N. J. (2009). Spatial and short-term temporal variations in Uranus' near-infrared spectrum. *Icarus*, 203:331–335.
- Orton, G. S., Aitken, D. K., Smith, C., Roche, P. F., Caldwell, J., and Snyder, R. (1987a). The spectra of Uranus and Neptune at 8-14 and 17-23 μm . *Icarus*, 70:1–12.
- Orton, G. S., Baines, K. H., Bergstralh, J. T., Brown, R. H., Caldwell, J., and Tokunaga, A. T. (1987b). Infrared radiometry of Uranus and Neptune at 21 and 32 μm . *Icarus*, 69:230–238.
- Orton, G. S., Encrenaz, T., Leyrat, C., Puetter, R., and Friedson, A. J. (2007). Evidence for methane escape and strong seasonal and dynamical perturbations of Neptune's atmospheric temperatures. *Astron. Astrophys.*, 473:L5–L8.
- Orton, G. S., Lacy, J. H., Achtermann, J. M., Parmar, P., and Blass, W. E. (1992). Thermal spectroscopy of Neptune: The stratospheric temperature, hydrocarbon abundances, and isotopic ratios. *Icarus*, 100:541–555.
- Podolak, M. and Marley, M. (1991). Interior model constraints on super-abundances of volatiles in the atmospheres of Neptune. *Bull. Am. Ast. Soc.*, 23:1164.

- Pollack, J. B., Rages, K., Pope, S. K., Tomasko, M. G., Romani, P. N., and Atreya, S. K. (1987). Nature of the stratospheric haze on Uranus: Evidence for condensed hydrocarbons. *J. Geophys. Res. Space Phys.*, 92:15037–15065.
- Pryor, W. R., West, R. A., Simmons, K. E., and Delistsky, M. (1992). High-phase-angle observations of Neptune at 2650 and 7500 Å: Haze structure and particle properties. *Icarus*, 99:302–317.
- Rages, K. A., Hammel, H. B., and Friedson, A. J. (2004). Evidence for temporal change at Uranus' south pole. *Icarus*, 172:548–554.
- Rayner, J. T., Tooney, D. W., Onaka, P. M., Denault, A. J., Stahlberger, W. E., Vacca, W. D., Cushing, M. C., and Wang, S. (2003). SpeX: A medium-resolution 0.8-5.5 micron spectrograph and imager for the NASA Infrared Telescope Facility. *Publ. Astron. Soc. Pac.*, 115:362–382.
- Rodgers, C. D. (1998). Information content and optimisation of high spectral resolution remote measurements. *Adv. Space Res.*, 21:361–367.
- Rosenqvist, J., Lellouch, E., Romani, P. N., Paubert, G., and Encrenaz, T. (1992). Millimeter-wave observations of Saturn, Uranus, and Neptune: CO and HCN on Neptune. *Astrophys. J.*, 392:L99–L102.
- Signorell, R. and Jetzki, M. (2007). Phase behavior of methane haze. *Phys. Rev. Lett.*, 98:013401.
- Sromovsky, L. A. and Fry, P. M. (2005). Dynamics of cloud features on Uranus. *Icarus*, 179:459–484.
- Sromovsky, L. A. and Fry, P. M. (2007). Spatially resolved cloud structure on Uranus: Implications of near-IR adaptive optics imaging. *Icarus*, 192:527–557.
- Sromovsky, L. A. and Fry, P. M. (2008). The methane abundance and structure of Uranus' cloud bands inferred from spatially resolved 2006 Keck grism spectra. *Icarus*, 193:252–266.

- Sromovsky, L. A., Fry, P. M., and Baines, K. H. (2002). The unusual dynamics of northern dark spots on Neptune. *Icarus*, 156:16–36.
- Sromovsky, L. A., Fry, P. M., Dowling, T. E., Baines, K. H., and Limaye, S. S. (2001). Coordinated 1996 HST and IRTF imaging of Neptune and Triton: III. Neptune’s atmospheric circulation and cloud structures. *Icarus*, 149:459–488.
- Sromovsky, L. A., Fry, P. M., Hammel, H. B., Ahue, W. M., de Pater, I., Rages, K. A., Showalter, M. R., and van Dam, M. A. (2009). Uranus at equinox: Cloud morphology and dynamics. *Icarus*, 203:265–286.
- Sromovsky, L. A., Fry, P. M., Hammel, H. B., de Pater, I., Rages, K. A., and Showalter, M. R. (2007). Dynamics, evolution, and structure of Uranus’ brightest cloud feature. *Icarus*, 192:558–575.
- Sromovsky, L. A., Fry, P. M., Limaye, S. S., and Baines, K. H. (2003). The nature of Neptune’s increasing brightness: Evidence for a seasonal response. *Icarus*, 163:256–261.
- Sromovsky, L. A., Irwin, P. G. J., and Fry, P. M. (2006). Near-IR methane absorption in outer planet atmospheres: Improved models of temperature dependence and implications for Uranus cloud structures. *Icarus*, 182:577–593.
- Strobel, D. F. (2005). Photochemistry in outer solar system atmospheres. *Space Sci. Rev.*, 116:155–170.
- Tyler, G. L., Sweetnam, D. N., Anderson, J. D., Borutzki, S. E., Campbell, J. K., Esheleman, V. R., Gresh, D. L., Gurrola, E. M., Hinson, D. P., Kawashima, N., Kursinski, E. R., Levy, G. S., Lindal, G. F., Lyons, J. R., Marouf, E. A., Rosen, P. A., Simpson, R. A., and Wood, G. E. (1989). Voyager radio science observations of Neptune and Triton. *Science*, 246:1466–1473.
- Vacca, W. D., Cushing, M. C., and Rayner, J. T. (2003). A method of correcting near-infrared spectra for telluric absorption. *Publ. Astron. Soc. Pac.*, 115:389–409.
- West, R. A., Baines, K. H., and Pollack, J. B. (1991). *Uranus*, chapter Clouds and aerosols in the Uranian atmosphere, pages 296–324. University of Arizona Press, Tucson.

Yelle, R. V., McConnel, J. C., Strobel, D. R., and Doose, L. R. (1989). The far ultraviolet reflection spectrum of Uranus: Results from the Voyager encounter. *Icarus*, 77:439–456.